Multiscale statistical characterization of migrating bed forms in gravel and sand bed rivers

Arvind Singh,[1] Stefano Lanzoni,[2] Peter R. Wilcock,[3] and Efi Foufoula-Georgiou[1]

Received 14 October 2010; revised 24 October 2011; accepted 25 October 2011; published 20 December 2011.

[1] Migrating bed forms strongly influence hydraulics, transport, and habitat in river environments. Their dynamics are exceedingly complex, making it difficult to predict their geometry and their interaction with sediment transport. Acoustic instrumentation now permits high-resolution observations of bed elevation as well as flow velocity. We present a space-time characterization of bed elevation series in laboratory experiments of sand and gravel transport in a large 84 m long, 2.75 m wide flume. We use a simple filtering and thresholding methodology to estimate bed form heights and report that the shape of their probability density function (pdf) remains invariant to discharge for both gravel and sand and has a positive tail slightly thicker than Gaussian. Using a wavelet decomposition, we quantify the presence of a rich multiscale statistical structure and estimate the scale-dependent celerity of migrating bed forms, showing the faster movement of smaller bed forms relative to the larger ones. The nonlinear dynamics of gravel and sand bed forms is also examined, and the predictability time, i.e., the interval over which one can typically forecast the system, is estimated. Our results demonstrate that flow rate as well as bed sediment composition exert a significant influence on the multiscale dynamics and degree of nonlinearity and complexity of bed form evolution.

Citation: Singh, A., S. Lanzoni, P. R. Wilcock, and E. Foufoula-Georgiou (2011), Multiscale statistical characterization of migrating bed forms in gravel and sand bed rivers, *Water Resour. Res.*, *47*, W12526, doi:10.1029/2010WR010122.

1. Introduction

[2] Sediment waves often occur in alluvial rivers as the result of the complex interactions and feedbacks between the turbulent flow field, sediment transport and the cohesionless bed. Depending on the bed shear stress and sediment grain size, the river bed can in general be either plane, or covered by ripples, dunes, bars, or antidunes. Among these bed forms, dunes and bars are the most common and their formation and evolution has important consequences not only for river management [*ASCE Task Force*, 2002], but also for the interpretation of the sedimentary structure [*Leclair*, 2002]. Bed form structure and dynamics is also recognized to exert considerable effects on biota and ecosystem river dynamics [e.g., *Yarnell et al.*, 2006].

[3] Dunes can form in both sand and gravel rivers, although they are more prevalent in sand bed systems. They usually form in the lower-flow regime (i.e., subcritical flow) and, under steady flow conditions, tend to reach a dynamic equilibrium state, whereby the average dune height, length and celerity remain approximately constant [*Coleman and Melville*, 1994]. Nevertheless, observational evidence indicates that continuous splitting and merging of dunes at different spatial scales characterizes this equilibrium [*ASCE Task Force*, 2002; *Wilbers*, 2004; *Parsons et al.*, 2005]. Smaller, faster migrating dunes are often observed to superimpose on larger, slower moving dunes. In some cases coalescence occurs, whereby two different dunes merge resulting in a new larger bed form [*Venditti et al.*, 2005]. Both superposition and coalescence affect the structure of the turbulent flow field, total flow resistance, and sediment transport [*Wilbers and ten Brinke*, 2003; *Schindler and Robert*, 2004; *Best*, 2005; *Fernandez et al.*, 2006; *McElroy and Mohrig*, 2009]. Observations also show that in rivers, dune fields are often three-dimensional [*Allen*, 1968], implying a flow pattern significantly different and much more complex than that established over two-dimensional dunes [*Barlow*, 1959; *Maddux et al.*, 2003; *Venditti*, 2007].

[4] Bars are observed in both sand and gravel bed rivers. They essentially consist of migrating alternating regions of scour and deposition with horizontal scales of the order of a few channel widths and vertical scales of the order of flow depth. These bars are formed as a result of a three-dimensional instability which gives rise to a stable periodic pattern [*Lanzoni*, 2000a, 2000b]. Both linear and weakly nonlinear theories have been developed to explain the development of these free bars in straight channels for the case of both bed load dominated and suspended load dominated sediment transport [*Blondeaux and Seminara*, 1985; *Colombini et al.*, 1987; *Federici and Seminara*, 2006].

[5] To predict the occurrence of bed forms and to characterize their geometrical properties, several approaches have been pursued to date. Empirical relationships were

[1]St. Anthony Falls Laboratory and National Center for Earth-surface Dynamics, Department of Civil Engineering, University of Minnesota, Twin Cities, Minneapolis, Minnesota, USA.
[2]Department IMAGE, University of Padova, Padua, Italy.
[3]Department of Geography and Environmental Engineering, Johns Hopkins University, Baltimore, Maryland, USA.

0043-1397/11/2010WR010122

first developed on the basis of flume experiments, relating the steady state bed form features (i.e., height, length and migration speed) to physical parameters such as flow intensity, flow depth, sediment size [see *Engelund and Fredsøe*, 1982; *Van Rijn*, 1984; *Coleman et al.*, 2006]. Since the seminal work of *Kennedy* [1963], several studies using stability analysis techniques were carried out to determine the critical conditions for bed form formation in the space of the relevant physical parameters [*Fredsøe*, 1974; *Blondeaux and Seminara*, 1985; *Colombini et al.*, 1987; *Ji and Mendoza*, 1997; *Colombini*, 2004; *Federici and Seminara*, 2006; *Colombini and Stocchino*, 2008]. More recently, increasingly refined numerical models have been developed to investigate the features of the turbulent flow field over fixed bed forms [*Maddux et al.*, 2003; *Nelson et al.*, 2005; *Tjerry and Fredsøe*, 2005] as well as the morphodynamic evolution of these bed forms, starting from a plane bed configuration and evolving toward an equilibrium state with bed forms of different scales continuously merging and splitting [*Defina*, 2003; *Federici and Seminara*, 2003; *Onda and Hosoda*, 2004; *Jerolmack and Mohrig*, 2005; *Giri and Shimizu*, 2006]. These latter morphodynamic models, although simplified, yield realistic and promising results, simulating successfully, important qualitative physical features of bed form evolution, including coalescence and asymmetric geometry.

[6] A parallel body of work has been devoted to understanding the statistical structure of bed forms at different scales. In sand bed rivers, spectral analysis of spatial and temporal bed elevation series [e.g., *Nordin and Algert*, 1966; *Hino*, 1968; *Jain and Kennedy*, 1974; *Engelund and Fredsøe*, 1982; *Nakagawa and Tsujimoto*, 1984; *Nikora et al.*, 1997; *Nikora and Goring*, 2001; *Aberle et al.*, 2010] has established the presence of a broad scaling regime (log-log linear spectrum) and a scale-dependent celerity of migrating sand dunes [e.g., *Exner*, 1931; *Raudkivi and Witte*, 1990; *Coleman and Melville*, 1994; *Nikora et al.*, 1997; *Schwämmle and Herrmann*, 2004; *Best*, 2005; *Jerolmack and Mohrig*, 2005]. In gravel bed rivers, the statistical properties of bed elevation fluctuations have only recently been analyzed and mostly on plane beds [*Nikora et al.*, 1998; *Marion et al.*, 2003; *Nikora and Walsh*, 2004; *Aberle and Nikora*, 2006]. To the best of our knowledge, the multiscale statistical structure of migrating gravel bed forms has not been investigated before, apart from the recent work of *Dinehart* [1992] and *Singh et al.* [2009a, 2010].

[7] The goal of this paper is to quantify the multiscale statistical structure of gravel and sand bed forms in order to gain insight into their complex dynamics and to develop metrics that can be used to quantitatively compare experimental, field, and modeling results. Comparison among bed forms is often based on average properties (i.e., mean bed form height, length and celerity). Bed form dynamics such as superposition and coalescence produce a complex statistical structure over a wide range of scales, indicating the need for refined but robust statistical descriptions. Advanced statistical analyses of bed elevations and bed forms are now possible given readily available high-resolution acoustic bed elevation instrumentation. Sand bed forms are clearly larger and more dynamic than gravel bed forms and an analysis of sand and gravel bed forms provides insight regarding statistical properties applied to both. To address these goals, we focus in this work on the multiscale statistical characterization of bed elevation series collected at multiple locations in large-scale steady state laboratory experiments in which gravel and sand are transported by a range of water discharges. We propose a filtering methodology for extracting bed forms and quantify the statistics of bed form heights in terms of their mean, variance and probability of exceedance. We use Fourier and wavelet spectra to estimate spectral slopes and scaling regimes, and wavelet cross-correlation analysis to estimate the scale-dependent celerity of bed forms. Finally, we propose a nonlinear analysis of the bed elevation series to quantify the degree of their complexity and infer the upper limits of predictability in relation to the three-dimensional elevation structure of the bed forms.

[8] The paper is structured as follows. In section 2 a brief review of the experimental setup is given. Physical characteristics of bed forms are presented in section 3. Section 4 presents the results of the Fourier and wavelet spectra and the scale-dependent wavelet cross-correlation analysis which leads to the estimation of the scale-dependent celerity. In section 5 higher-order structure functions (capturing the whole probability density function (pdf)) of the bed elevation increments are computed and their scaling parameterized. Section 6 presents a nonlinear analysis of bed elevation series to quantify the complexity of bed form evolution beyond linear statistics using a phase-space representation. Finally, a summary of the present work and concluding remarks are presented in section 7.

2. Experimental Setup and Data Collected

2.1. Experimental Setup

[9] The experiments reported here were conducted in the Main Channel facility of the St. Anthony Falls laboratory, University of Minnesota. The flume in the Main channel facility is 84 m long, 2.75 m wide and 1.8 m deep. The flume used a water feed from the Mississippi River and was operated with a sediment recirculation system that allowed continuous monitoring of the sediment transport rates. The sediment flux monitoring system was located at 55 m from the upstream end of the flume and was composed of five adjacent, identical aluminum weigh pans (positioned 0.55 m apart) that spanned the width of the channel and independently measured the submerged weight of the sediment intercepted by the bed load trap. The sediment recirculation system was capable of entraining and recirculating particles up to 76 mm in size. Water discharge was measured using a sharp crested weir located 18 m downstream of the bed load trap. The water depth within the channel was regulated by sharp crested weir, which acted as a tail gate. Water level was continuously recorded using an acoustic sensor. The maximum discharge capacity of the channel was 8000 L s^{-1}.

[10] In the case of gravel bed experiments, the entire channel bed was covered with a 45 cm thick layer of sediment composed of a mixture of 85% gravel (median particle size diameter, $d_{50} = 11.3$ mm) and 15% sand (median particle size diameter, $d_{50} = 1$ mm). The final grain size distribution obtained in the gravel bed experiment after mixing the sediment had a $d_{50} = 7.7$ mm, $d_{16} = 2.2$ mm and $d_{84} = 21.2$ mm [*Singh et al.*, 2010]. In the case of sand bed experiments, the first 35 m of the flume consisted of a fixed concrete bed, while the remaining downstream 20 m

reach of the channel was filled with a 45 cm thick layer of uniform sand with median grain size diameter $d_{50} = 1$ mm, $d_{16} = 0.75$ mm and $d_{84} = 1.42$ mm. In both series of experiments, the mean specific density of sediment was ~2.65.

[11] Prior to the data collection, a constant water discharge Q was fed into the channel to achieve quasi-dynamic equilibrium in transport and slope adjustment for both water surface and sediment bed. The assessment of this dynamic equilibrium state was evaluated by checking the stability of the 60 min average total sediment flux at the downstream end of the channel. Using the pan accumulation data, the acquisition software computed a 60 min mean of sediment flux in all five pans. Dynamic equilibrium was assumed to be reached when variation in this value became negligible. In other words, when the average of the previous 60 min of instantaneous flux values computed from the pan data stabilized, we determined the channel to be in dynamic equilibrium and proceeded with formal data collection and sampling. Moreover, the tail gate at the end of the flume was suitably adjusted in order to ensure that the water surface and the channel bed were nearly parallel, thus minimizing nonuniform flow. The water surface and the bed surface slopes in the case of gravel bed experiments were determined using the DAQ system which measured simultaneously the water surface and the bed surface elevations at a high resolution (see *Singh et al.* [2010] for details about the DAQ system), whereas for the sand bed experiments, they were determined through the measurements of water surface elevation and flow depth monitored at three different locations in the channel along the flow direction. After attaining equilibrium, experiments were ran for a period of approximately 15 h for sand bed tests and 20 h for gravel bed tests, during which time data were collected. More details about the experimental setup are given by *Singh et al.* [2009a].

2.2. Data Collected

[12] The data considered here are the temporal series of bed elevations collected at several locations of the channel as well as sediment transport rates measured at the downstream end of the flume (see Figure 1). The bed elevation was measured through seven stationary submersible sonar transducers of 2.5 cm diameter, mounted at the end of rigid steel tubes, of diameter 1.5 cm. The transducers were placed approximately 0.3 m above the mean bed elevation, and were directed perpendicular to the bed. The spatial locations of the sonar probes are depicted in Figure 1 for both the gravel (Figure 1a) and sand (Figure 1b) bed experiments. In all experiments, the first five sonars (G1 to G5 in gravel and S1 to S5 in sand) were located 0.95 m upstream of each of the five pans used to collect and weigh the transported sediment. For the gravel bed experiments, sonars G6 and G7 were located 1.21 m upstream of sonars G2 and G4, respectively (see Figure 1a). In the sand bed experiments, sonars S6 and S7 were set along the centerline of the channel, at distances of 7 and 12 m upstream of S3, respectively. Sonars sampled bed elevation every 5 s for the gravel bed experiments and 10 s for the sand bed experiments, with a vertical precision of ~1 mm. The acquisition time was synchronized with that of the sediment accumulation data. In order to avoid data potentially impacted by wall effects, sonars G1 and G5 and S1 and S5 were not considered in the analysis (see Table 1 the mean and the standard deviation of the bed form heights computed from

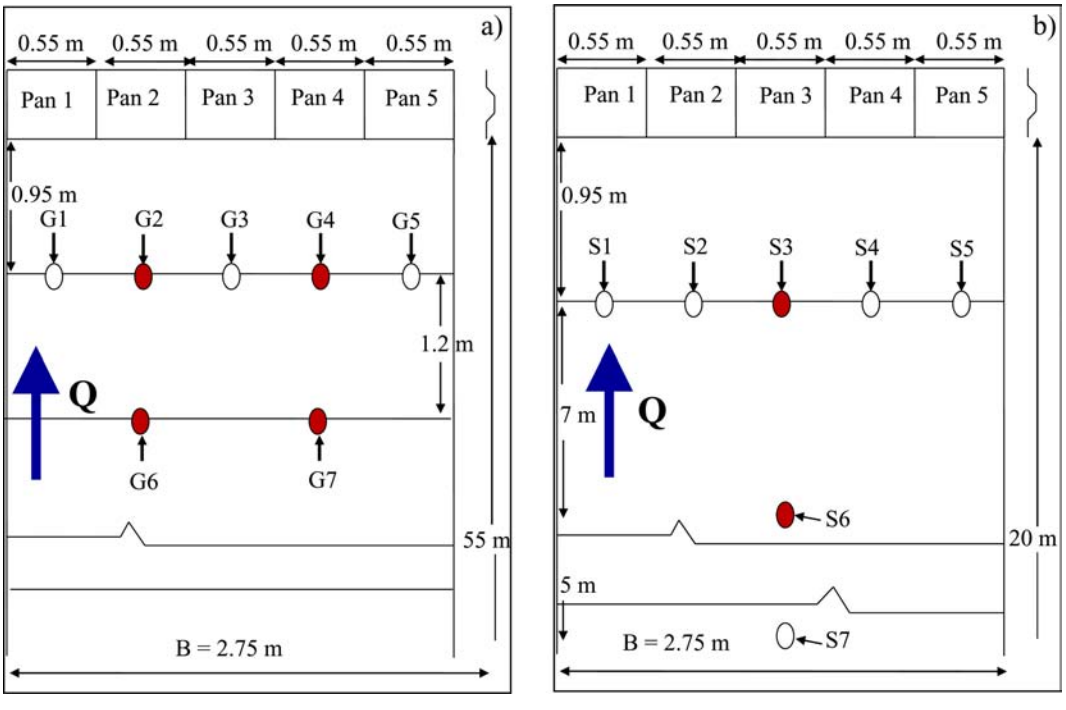

Figure 1. Schematic diagram of probe locations and distances in the experimental channel of the St. Anthony Falls Laboratory at the University of Minnesota for (a) the gravel bed experiments and (b) the sand bed experiments. Solid dots represent the pair of probes (upstream to downstream) used in the cross-correlation analysis.

Table 1. Hydraulic Conditions and Statistics of Bed Forms[a]

Experiment	Q_w (L s^{-1})	D (m)	v (m s^{-1})	S_w	R_H (m)	Shear Velocity u_b^* (m s^{-1})	Probes[b]	ave(h_b) (cm)	SD(h_b) (cm)	$\overline{\text{ave}(h_b)}$ (cm)	$\overline{\text{SD}(h_b)}$ (cm)
Gravel	2000	0.55	1.32	0.0019	0.39	0.102	(G1)	2.79	1.18	4.77	1.83
	2000	0.55	1.32	0.0019	0.39	0.102	G2	5.06	1.74	4.77	1.83
	2000	0.55	1.32	0.0019	0.39	0.102	G3	5.45	2.14	4.77	1.83
	2000	0.55	1.32	0.0019	0.39	0.102	G4	4.45	1.73	4.77	1.83
	2000	0.55	1.32	0.0019	0.39	0.102	(G5)	2.78	1.14	4.77	1.83
	2000	0.55	1.32	0.0019	0.39	0.102	G6	4.17	1.49	4.77	1.83
	2000	0.55	1.32	0.0019	0.39	0.102	G7	4.73	2.03	4.77	1.83
	2800	0.64	1.59	0.0029	0.44	0.135	(G1)	8.25	3.49	8.23	2.79
	2800	0.64	1.59	0.0029	0.44	0.135	G2	8.24	2.69	8.23	2.79
	2800	0.64	1.59	0.0029	0.44	0.135	G3	8.34	2.97	8.23	2.79
	2800	0.64	1.59	0.0029	0.44	0.135	G4	9.23	2.95	8.23	2.79
	2800	0.64	1.59	0.0029	0.44	0.135	(G5)	7.45	2.67	8.23	2.79
	2800	0.64	1.59	0.0029	0.44	0.135	G6	7.02	2.61	8.23	2.79
	2800	0.64	1.59	0.0029	0.44	0.135	G7	8.32	2.76	8.23	2.79
Sand	2500	1.25	0.73	0.0021	0.65	0.161	(S1)	10.12	4.39	11.43	5.17
	2500	1.25	0.73	0.0021	0.65	0.161	S2	10.23	3.83	11.43	5.17
	2500	1.25	0.73	0.0021	0.65	0.161	S3	9.93	4.07	11.43	5.17
	2500	1.25	0.73	0.0021	0.65	0.161	S4	14.54	7.09	11.43	5.17
	2500	1.25	0.73	0.0021	0.65	0.161	(S5)	15.73	6.81	11.43	5.17
	2500	1.25	0.73	0.0021	0.65	0.161	S6	11.02	5.68	11.43	5.17
	2500	1.25	0.73	0.0021	0.65	0.161	(S7)	10.26	3.50	11.43	5.17
	3200	1.21	0.96	0.0028	0.64	0.182	(S1)	15.95	7.01	13.84	5.00
	3200	1.21	0.96	0.0028	0.64	0.182	S2	12.31	5.23	13.84	5.00
	3200	1.21	0.96	0.0028	0.64	0.182	S3	13.86	5.33	13.84	5.00
	3200	1.21	0.96	0.0028	0.64	0.182	S4	14.24	4.11	13.84	5.00
	3200	1.21	0.96	0.0028	0.64	0.182	(S5)	18.95	5.43	13.84	5.00
	3200	1.21	0.96	0.0028	0.64	0.182	S6	14.95	5.31	13.84	5.00
	3200	1.21	0.96	0.0028	0.64	0.182	(S7)	8.31	3.96	13.84	5.00

[a]The probe locations are given in Figure 1. Q_w is water discharge (L s^{-1}), D is average depth of flow in test section (m), v is velocity of flow computed using flow depth and flume width (m s^{-1}), R_H is hydraulic radius (m), S_w is water surface slope, u^*_b is the shear velocity (computed using $\sqrt{(gDS_w)}$, where g is the acceleration due to gravity and is 9.81 m s^{-2}), ave(h_b) is the mean bed form height (cm), SD(h_b) is the standard deviation of bed form heights (cm), $\overline{\text{ave}(h_b)}$ is the average of bed form height over probes G2, G3, G4, G6, and G7 for gravel bed experiments and probes S2, S3, S4, and S6 for sand bed experiments (cm), $\overline{\text{SD}(h_b)}$ is the average of standard deviations of bed form heights over probes G2, G3, G4, G6, and G7 for gravel bed experiments and probes S2, S3, S4, and S6 for sand bed experiments (cm).

[b]Note that the probes in the parentheses have not been used in the analysis.

the sonars which attest the presence of a wall bias). The data collected by sonar S7 in the sand bed experiments were also disregarded, owing to the upstream effects induced by the fixed concrete bed, located about 7 m (i.e., ~2.5 times the channel width) upstream of S7. Sediment transport rates were measured through the bed load traps at a sampling interval of 1.1 s.

[13] The experiments documented here covered a range of bed form–producing discharges. Specifically, we considered the data collected for the discharges of 2000 and 2800 L s^{-1} for gravel and 2500 and 3200 L s^{-1} for the sand bed experiments. The relevant hydraulic conditions characterizing these experiments are given in Table 1.

3. Physical Characteristics of Bed Forms

3.1. Three-Dimensional Nature of Bed Forms

[14] Figure 2 shows the pictures of the experiments depicting the bed forms formed in the gravel bed (Figure 2a) and in the sand bed (Figure 2b) for the discharges of 2800 and 2500 L s^{-1}, respectively. The observed gravel bed forms were transitioning from two-dimensional to three-dimensional at the discharge of 2000 L s^{-1} and were fully three-dimensional at the discharge of 2800 L s^{-1}, whereas the sand bed forms were primarily three-dimensional for both the discharges. This three-dimensionality can be appreciated from the time series of bed elevations reported in Figures 3 (left) (for gravel) and 4 (left) (sand), which show the simultaneously sampled bed elevations at probes G2, G3, G4, and G7 (gravel bed) and probes S2, S3, S4, and S6 (sand bed). Figure 3 (right) shows the increments of the

Figure 2. Bed forms formed in the main channel facility at the St. Anthony Falls Laboratory for (a) the gravel bed experiment at the discharge of 2800 L s^{-1} and (b) sand bed experiments at the discharge of 2500 L s^{-1}. The flow direction in Figure 2a is from top to bottom, and in Figure 2b it is from bottom to top.

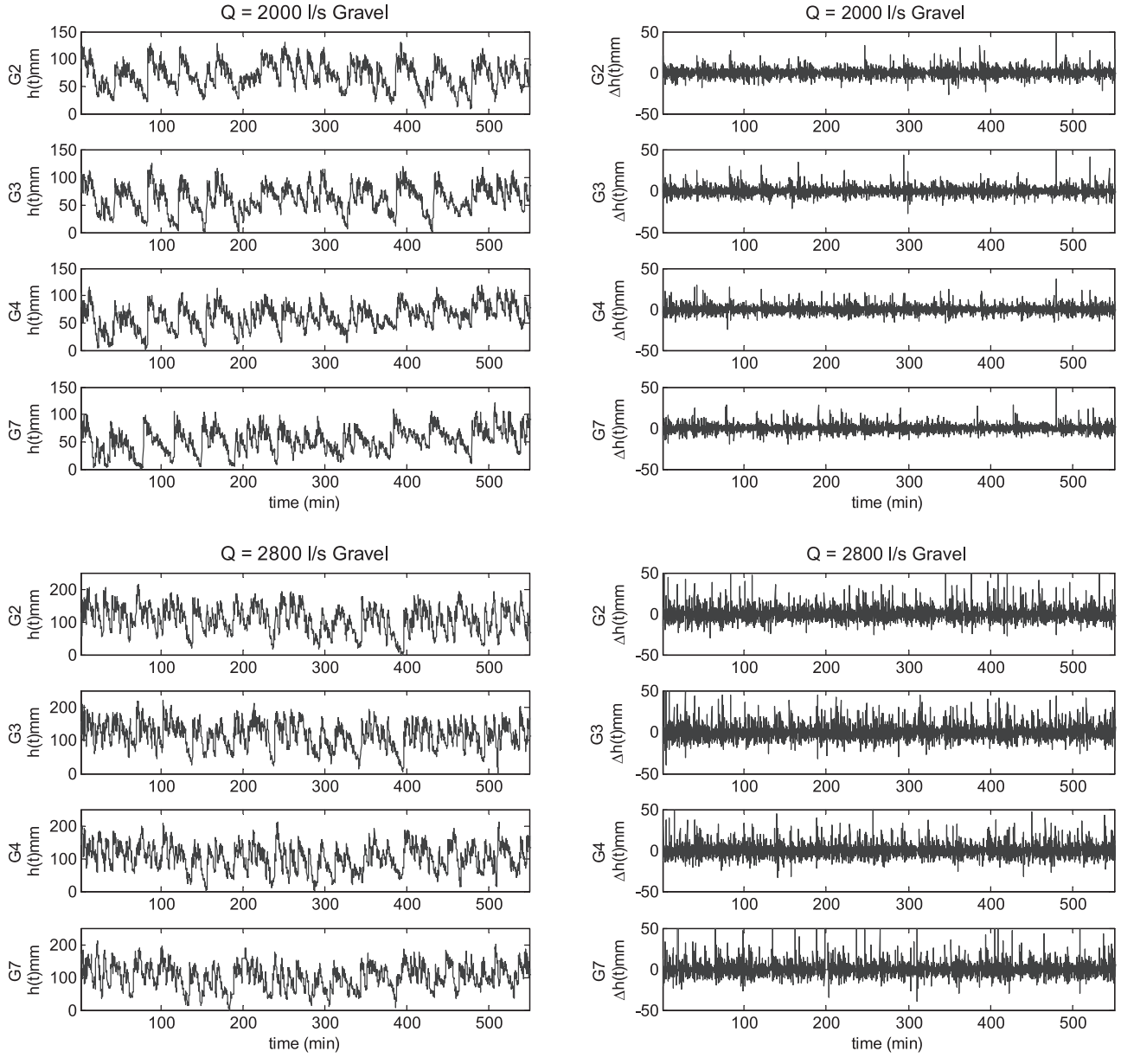

Figure 3. Time series of (left) bed elevation $h(t)$ and (right) bed elevation increments $\Delta h(t) = h(t+1) - h(t)$ for gravel bed experiments for discharge of (top) 2000 and (bottom) 2800 L s^{-1} at four different locations for each discharge (see Figure 1a for probe locations).

bed elevation series (increments $\Delta h(t)$ here defined as the difference between adjacent values see also discussion in section 5.1) for the gravel bed, whereas Figure 4 (right) shows the increments of the bed elevation for the sand bed experiment. Close visual inspection of Figures 3 (left) and 4 (left) reveals a lateral variation in bed form structure. This lateral variation can be better appreciated by computing the difference in simultaneously sampled signals located in line across the width of the channel, i.e., in a line perpendicular to the channel centerline. Such a plot is shown in Figure 5, in which the time series difference of simultaneously sampled bed elevations at the locations of probes G2, G3, and G4 and S2, S3, and S4 across the width of the channel are shown for the gravel bed experiments (Figures 5a and 5b) and the sand bed experiments (Figures 5c and 5d) for the discharges of 2000 L s^{-1} (Figure 5a), 2800 L s^{-1} (Figure 5b), 2500 L s^{-1} (Figure 5c), and 3200 L s^{-1} (Figure 5d). In the case of two-dimensional bed forms the time series of bed elevation differences should be laterally consistent. However, this is not the case in any of the bed configurations.

[15] The gravel bed experiments, exhibiting an aspect ratio (ratio of flume width to flow depth) of 4.3 for the discharge of 2000 L s^{-1} and 5 for the discharge of 2800 L s^{-1}, were characterized by the formation of dunes and by the presence of diagonal fronts indicating the possible presence of incipient bars [*Lanzoni*, 2000a, 2000b] as well as sorting waves with distinct coarse fronts of one or two coarse grain heights (Figure 2a). For the lower discharge (2000 L s^{-1}), the bed shows three dimensional, relatively small bed forms, as documented by the elevation differences of Figure 5a.

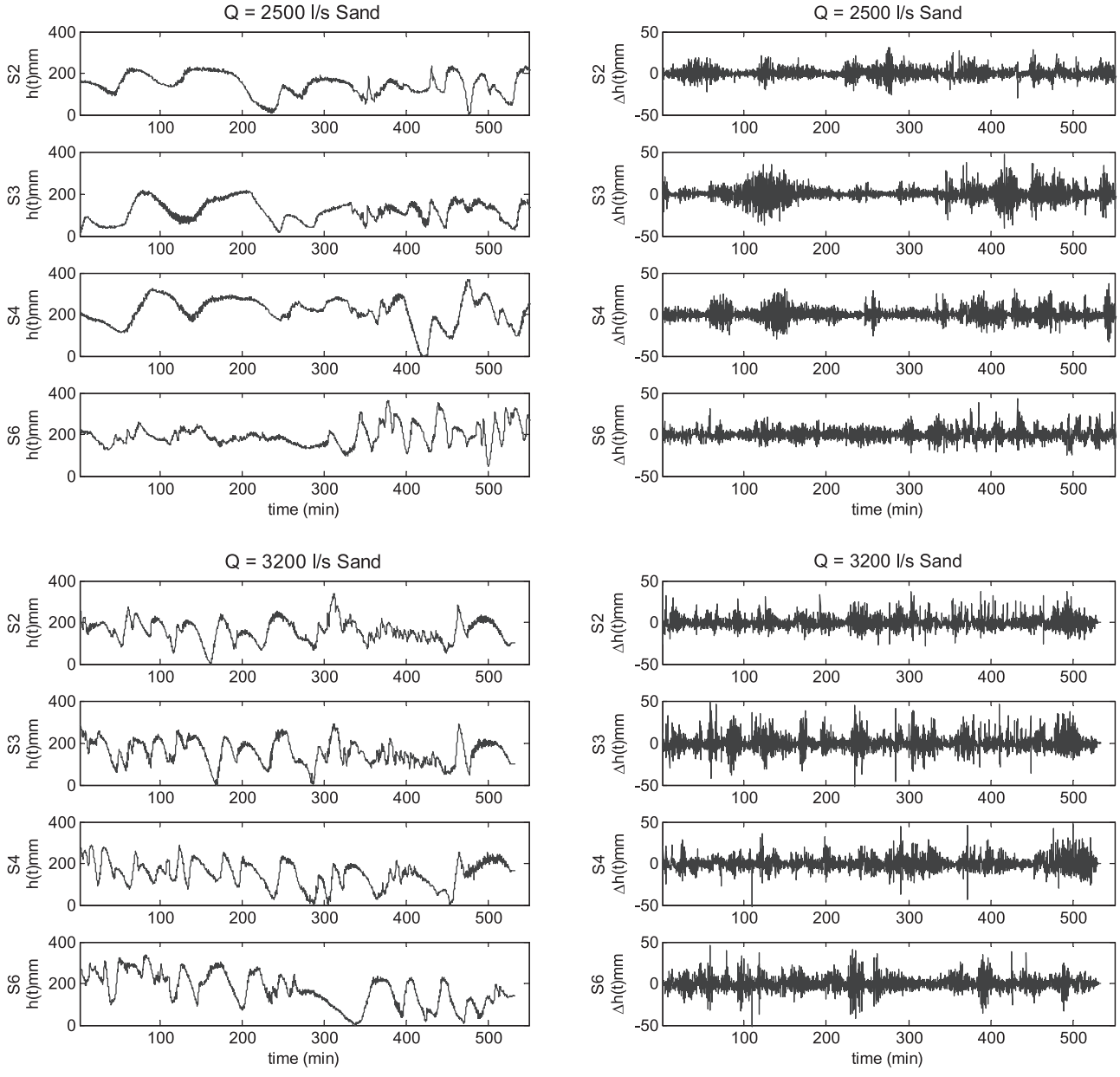

Figure 4. Time series of (left) bed elevation $h(t)$ and (right) bed elevation increments $\Delta h(t) = h(t+1) - h(t)$ for sand bed experiments for discharge of (top) 2500 and (bottom) 3200 L s^{-1} at four different locations for each discharge (see Figure 1b for probe locations).

For the higher discharge (2800 L s^{-1}), the bed form height and degree of three-dimensionality increases (Figure 5b).

[16] In the case of the sand bed experiments, dunes were observed and were of the order of 3–5 m in length and 1–2 m in width (Figure 2b). In particular, Figure 2b suggests that in the sand bed experiments there were approximately 1–2 bed forms of characteristic size per cross section of the channel. An issue that arises is whether these bed forms were constrained by the flume walls and the width to depth (aspect) ratio of the experimental setting. *Crickmore* [1970] demonstrated experimentally that the aspect ratio plays an important role in bed form development and, in fact, bed form height, length and spectral width were observed to decrease as the channel width became comparable with that of the bed forms. In particular, by decreasing the width to depth ratio from 8.4 to 2.4, all the other quantities being almost unchanged, *Crickmore* [1970] found that the decrease in bed form height turned out to be of the order of 10%–20%. Moreover, channel narrowing was observed to inhibit short bed form wavelengths and imparting a strong two-dimensional character to bed features. In principle, the reproduction of the actual geometry of natural dunes then requires very large, unpractical experimental installations and hence field investigations, such as those carried out by *Nikora et al.* [1997]. Nevertheless, laboratory flumes provide controlled experimental conditions which usually help data analysis and interpretation. The aspect ratio attained in the present sand bed experiments is 2.2 and 2.27 for the discharges of 2500 and 3200 L s^{-1}, respectively, and is similar to the smallest one investigated by *Crickmore* [1970]. The

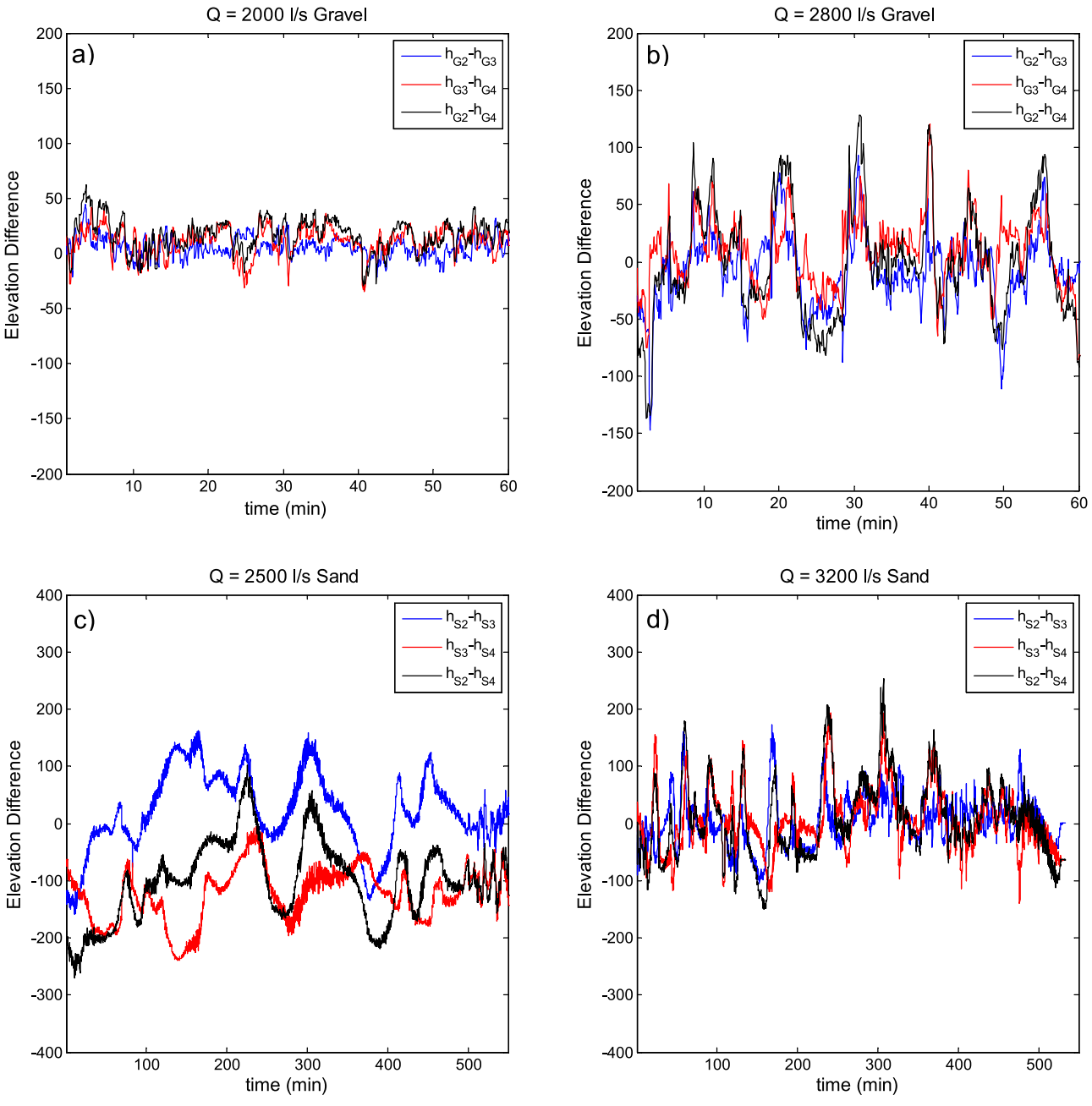

Figure 5. Time series of differences of simultaneously sampled bed elevations at probes G2, G3, and G4 across the width of the channel for the gravel bed experiments (Figures 5a and 5b) and probes S2, S3, and S4 for the sand bed experiments (Figures 5c and 5d) for discharge of (a) 2000, (b) 2800, (c) 2500, and (d) 3200 L s^{-1}. Note that in the case of two-dimensional bed forms the bed elevation differences at probes located in-line across the width of the channel as a function of time would be constant.

observed sand dunes then should be smaller and shorter than those attained in a larger channel. However, we note that the overall bed configuration shown in our Figure 2b is much more similar to that obtained by *Crickmore* [1970] for the intermediate aspect ratio (4.8); that is, it does not exhibit a clear two-dimensional structure as that observed in *Crickmore*'s [1970] narrower channel. This suggest that, despite the low aspect ratios here investigated, the flume width is likely large enough to include at least the width of a typical bed form unit, thus implying a reduced width dependence. In particular, the observed dune wavelength turns out to be lower than those estimated according to the *Van Rijn* [1984] and *Julien and Klassen* [1995] predictors, which yield a dune length of the order of 6.2–7.3 times the flow depths and therefore about 2.8–3.2 times the channel width in the present sand bed experiments.

3.2. Extraction of Bed Form Heights

[17] A fundamental difficulty in studies concerning bed form dynamics is to decide on an objective method for characterizing the geometry of the various bed form units [*Crickmore*, 1970; *Klaassen*, 1990; *Julien and Klassen*,

1995; *van der Mark et al.*, 2008]. Figure 6a shows the bed elevation observed for the gravel bed experiment at the location of probe G2 for the discharge of 2000 L s^{-1}, while Figure 6f shows the bed elevation observed at the location of Probe S3 at a discharge of 3200 L s^{-1} for the case of the sand bed experiment (see the sketch in Figure 1 for probe locations). To obtain a reliable measure of bed form heights, the high-frequency fluctuations associated with the presence of very small bed forms, were filtered out from the bed elevation signal $h(t)$ using the Fourier transform (Figures 6b and 6g). The local maxima and the local minima in the filtered signal were then determined (Figures 6c and 6h) and the differences between consecutive local minima and local maxima were computed. Finally, to obtain an estimate of the average bed form height, the bed form heights above a certain threshold were extracted. The threshold was assumed to be 25% of the maximum bed form height at that particular discharge and location [*Klaassen*, 1990]. Figures 6d and 6e (gravel) and 6i and 6j (sand) show the distribution of bed form heights before and after this extraction. The summary of the statistics of bed form heights for both gravel and sand bed experiments, collected at different probe locations, are shown in Table 1. From Table 1 it can be seen that the mean bed form height increases with increasing discharge for both gravel and sand bed experiments. For example, the mean bed form heights are about 5 and 8 cm for the discharges of 2000 and 2800 L s^{-1}, respectively, for the gravel bed experiments, whereas they are about 11 and 14 cm for the discharges of 2500 and 3200 L s^{-1}, respectively, for the sand bed experiments. Note that, in the case of the gravel bed experiments, the values of mean bed form heights are similar to those obtained from high-resolution longitudinal profiles (not shown here) surveyed at the end of the experiments. These longitudinal profiles also indicate that the bed form wavelength is ~4 m for both discharges.

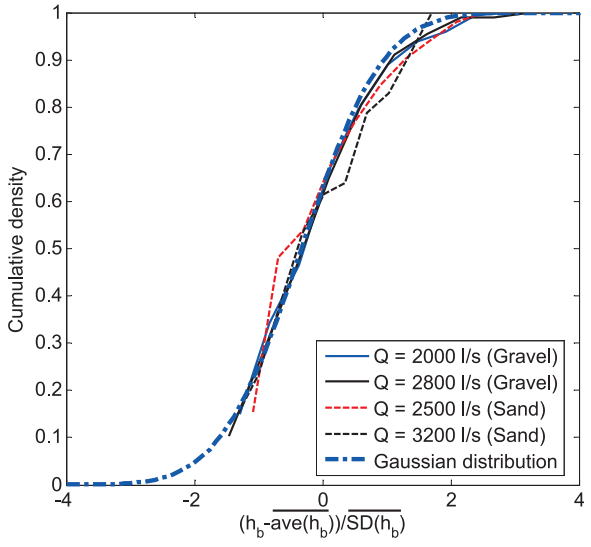

Figure 7. Cumulative density function of bed form heights obtained from the time series of bed elevation (see section 3.2 for explanation of the bed form extraction). Note that the distribution of bed form heights for each discharge was obtained from the ensemble of bed form heights extracted from all the probes at that particular discharge excluding the probes in parentheses in Table 1.

[18] Figure 7 shows the cumulative frequency histograms of the standardized bed form heights $((h_b - \mathrm{ave}(h_b))/\mathrm{SD}(h_b))$ for the gravel and the sand bed experiments, where

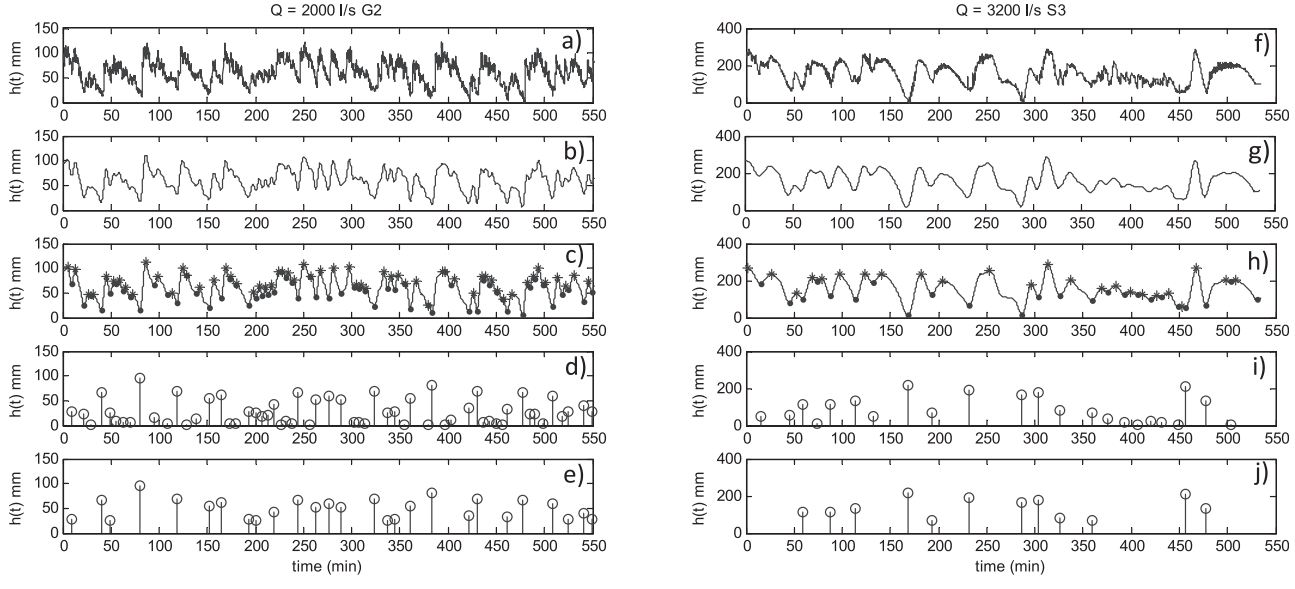

Figure 6. Time series (a, f) of bed elevation, (b, g) filtered bed elevation using Fourier transform, (c, h) bed elevation showing the location of local maxima and local minima, (d, i) extracted bed form heights, and (e, j) extracted bed form heights above a certain threshold for (left) the gravel bed experiment and (right) the sand bed experiment at a discharge of 2000 and 3200 L s^{-1}, respectively. Note that the sampling time for the bed elevation in the gravel bed experiments was 5 s, while for sand bed experiments it was 10 s. See text for more explanation.

h_b denotes the bed form height, ave(.) and SD(.) denote the mean and the standard deviation of bed form heights for each probe and $\overline{(.)}$ denotes the average of bed form quantities (mean and standard deviation) over different probe locations. Interestingly, it is observed that the distribution of bed form heights does not change in shape for gravel and sand and that the positive tails are slightly thicker than those of the Gaussian distribution (shown for comparison in Figure 7). In a recent study *van der Mark et al.* [2008] showed that the Gaussian, Gamma, and Weibull distributions provide the best approximation for the bed form heights; however, in that study the bed form heights were extracted from bed elevation profiles not from elevation time series as done in our study.

[19] The mean values of bed form heights reported in Table 1, indicate that the differences between the bed form height estimated from probes located along the same longitudinal coordinate (probes G2 and G6 and G4 and G7 for the gravel bed experiments and probes S3 and S6 for the sand bed experiments) are at maximum of the order of l–2 cm. As discussed before, probes 1 and 5 are affected by the wall for both gravel and sand bed experiments. Indeed, their mean and standard deviation of bed form heights (reported in Table 1) show appreciable deviation from the mean and the standard deviation of bed form heights estimated at other probe locations, specifically, for probes G1 and G5 at 2000 L s^{-1} for the gravel bed experiment and S1 and S5 at 3200 L s^{-1} for the sand bed experiment. The distribution of bed form heights provided by all the other probes suggests a substantially spatially homogeneous behavior of bed forms.

4. Scale-Dependent Bed Form Migration

[20] Section 4 presents the results of a multiscale analysis of bed form geometry and dynamics for the gravel and sand experiments under different flow conditions. Emphasis is placed on localized time-frequency analysis which can accurately estimate energy distribution across scales and quantify scale-dependent dynamics. The readers familiar with the methodologies of wavelet spectrum and cross-correlation analysis can go directly to section 4.2.

4.1. Overview of Wavelet Spectra and Cross-Correlation Analysis

4.1.1. Wavelet Transform

[21] For signals that exhibit multiple scales of variability and frequency content that changes with time, a localized (e.g., via wavelets) versus global (Fourier) analysis is often insightful. The wavelet transform of a function $h(t)$ is defined as the integral transform with a series of functions $\psi_{a,b}(t)$, i.e.,

$$W_{h(t)}(a,b) = \int_{-\infty}^{+\infty} h(t)\psi_{a,b}(t)dt, \tag{1}$$

where the functions $\psi_{a,b}$, called wavelets, are obtained from the "mother" wavelet $\psi(t)$ by translation and scaling, i.e.,

$$\psi_{a,b}(t) = \frac{1}{\sqrt{a}}\psi\left(\frac{t-b}{a}\right); \qquad a > 0; \qquad b \in R. \tag{2}$$

Here a is the scaling parameter and b is the location parameter. The factor $1/\sqrt{a}$ is a normalizing constant chosen to ensure that the $\mathcal{L}^2$ norm is preserved [e.g., *Mallat*, 1998; see also *Kumar and Foufoula-Georgiou*, 1997].

[22] For the wavelet transform to be invertible, the mother wavelet must have finite support and satisfy the admissibility condition $\int_{-\infty}^{+\infty} \psi(t)dt = 0$, i.e., it must have area under the curve zero (which makes it a kind of local differencing filter). Wavelets with higher-order vanishing moments i.e., $\int_{-\infty}^{+\infty} t^k\psi(t)dt = 0, (k = 0, 1, 2, \ldots, N-1)\infty$, where N is the order of vanishing moment, are possible, resulting in higher-order differencing filters which can remove polynomial trends from a signal. For example, it can be shown [e.g., *Kumar and Foufoula-Georgiou*, 1997] that a wavelet with N vanishing moments removes a polynomial trend of order $(N-1)$. That is, if $N = 1$ the wavelet acts as a first-order differencing filter and removes a constant value trend; if $N = 2$, the wavelet acts as a second-order differencing filter removing a linear trend, and so on. A commonly used mother wavelet is the family of Gaussian-based wavelets defined as the Nth-order derivatives of a Gaussian function $g_0(t)$, i.e., $g_N(t) = (d^N/dt^N)g_0(t)$, $(N = 1, 2, \ldots)$, where N is the order of derivative. It is noted that $g_N(t)$ has N vanishing moments and that for $N = 2$ the wavelet is the well known Mexican hat wavelet removing a piecewise linear trend from the signal. In this study, the fluctuations (wavelet coefficients) of bed elevations at various scales were computed using the Mexican hat wavelet $g_2(t)$ as the mother wavelet:

$$g_2(t) = \frac{2}{\sqrt{3}}\pi^{-1/4}(1-t^2)e^{-t^2/2}. \tag{3}$$

[23] In other words, substituting equation (3) into (1) and (2), the wavelet coefficients (WC) at location b and scale a were obtained as

$$\mathrm{WC}(a,b) = \frac{1}{\sqrt{a}}\int_{-\infty}^{+\infty} h(t)g_2\left(\frac{t-b}{a}\right)dt. \tag{4}$$

4.1.2. Wavelet Spectrum

[24] It is important to note that the wavelet transform provides a localized decomposition of the signal as opposed to the Fourier transform which is a global filtering operation. As such, the relative contribution of the signal energy contained at a specific scale a and location b is given by the two-dimensional wavelet energy density function:

$$E(a,b) = |W_{h(t)}(a,b)|^2. \tag{5}$$

A plot of $E(a,b)$ is known as the scalogram. Integrating over all locations b, one obtains the wavelet power spectrum

$$\mathrm{WS}_{h(t)}(a) = \int_{-\infty}^{+\infty} |W_{h(t)}(a,b)|^2 db. \tag{6}$$

One can convert the scale-dependent wavelet energy spectrum into a frequency-dependent wavelet energy spectrum $WS_{h(t)}(f)$ in order to compare it with the Fourier spectrum of the signal. To do this, we assign to the scale a a characteristic frequency which is typically the band-pass center of the wavelet's power spectrum. For the Mexican hat wavelet, the band pass frequency at scale a is $f_c = 0.251/a$ (see Figure 8) [see also *Addison*, 2002]. Because of the frequency distribution within each wavelet, the wavelet spectrum is smeared compared with the Fourier spectrum. At the same time, the wavelet filter interrogates the signal locally and as such it correlates its shape with specific local features of the signal making it a more accurate metric for the energy distribution over scales (frequencies) [e.g., *Gamage and Blumen*, 1993; *Hudgins et al.*, 1993]. A comparison of the Fourier and wavelet spectra for the bed elevation series will be demonstrated in section 4.1.3.

4.1.3. Wavelet Cross Correlation

[25] Cross-correlation analysis enables the statistical determination of the degree of waveform similarity between two stationary time series. The cross-correlation coefficient provides a quantitative measure of the linear dependence between two signals as they are progressively shifted in time with respect to each other. A standard two point cross correlation between two signals, $h_1(t)$ and $h_2(t)$, is defined as

$$C_{h_1,h_2}(\Delta t) = \frac{E\{[h_1(t) - \overline{h_1(t)}][h_2(t+\Delta t) - \overline{h_2(t)}]\}}{\sigma_{h_1(t)}\sigma_{h_2(t)}}, \quad (7)$$

where t is the time, Δt is the time lag, $\overline{h_1(t)}$ and $\overline{h_2(t)}$ denote the mean values, and $\sigma_{h1(t)}$ and $\sigma_{h2(t)}$ denote the standard deviations of $h_1(t)$ and $h_2(t)$, respectively.

[26] For two bed elevation time series observed at distance L apart, the standard cross-correlation analysis can be used to estimate the average bed form celerity using the time lag that results in the maximum correlation between the two series (assuming that peak correlation captures, in a statistical sense, the passage of the same bed form). The bed form celerity (velocity) can then be estimated as $v_c(a, \Delta t) = L/\Delta t_{[\max]}$, where a is the scale (wavelength of bed form), L is the distance between the two probes, and $\Delta t_{[\max]}$ is the Δt such that $C_{h_1,h_2}(\Delta t_{[\max]}) = \max[C_{h_1,h_2}(\Delta t), \forall \Delta t]$.

[27] Since bed elevation series are known to contain energy (variability) at multiple scales, cross-correlation analysis at multiple scales is expected to offer valuable insight. The most efficient way to perform such an analysis is via wavelets.

[28] The wavelet cross covariance (WCC) between two signals $h_1(t)$ and $h_2(t)$ can be computed as

$$\mathrm{WCC}_{h_1,h_2}(a, \Delta t) = \int_{-\infty}^{+\infty} W_{h_1}(a, b) W_{h_2}(a, b + \Delta t) db, \quad (8)$$

where $W_{h_1}(a, b)$ and $W_{h_2}(a, b + \Delta t)$ are the wavelet coefficients of $h_1(t)$ and $h_2(t)$, respectively, at scale a and two adjacent locations b and $b + \Delta t$, respectively. The wavelet cross correlation can be obtained by appropriate normalization by the variance of the signals. This wavelet cross correlation can then be used to estimate the bed form celerity as a function of scale as demonstrated in section 4.2.

4.2. Gravel Bed Topography Analysis

4.2.1. Wavelet Spectra

[29] Various studies [e.g., *Nikora et al.*, 1998; *Butler et al.*, 2001; *Marion et al.*, 2003; *Nikora and Walsh*, 2004; *Aberle and Nikora*, 2006; *Singh et al.*, 2009a, 2010] have reported the scaling properties of gravel bed topography using spectral analysis or structure function analysis, i.e., analysis of the statistical moments of bed elevation increments at different scales. The scaling exponent $2H$ of the second-order structure function (variance of increments) relates to the spectral slope β via the relationship $\beta = 2H + 1$, where H is the so-called Hurst exponent. *Nikora et al.* [1998] found that the scaling exponent $H = 0.79$ for natural beds was significantly higher than for unworked beds, $H = 0.5$. Spectral slopes in gravel bed topography series have been reported to be of the order of $\beta = 1.9 - 2.2$ which correspond to $H = 0.45 - 0.6$ [e.g., *Singh et al.*, 2010].

[30] As discussed in section 4.1, the wavelet transform of a signal provides a local interrogation of the frequency content of the signal at different scales. At each scale a, by integrating over all locations the squared magnitude of the local wavelet coefficients (equation (6)), one depicts the

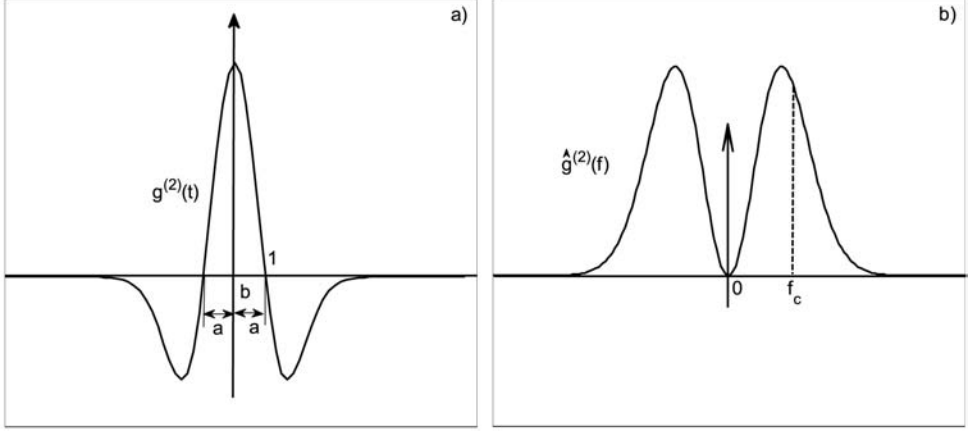

Figure 8. (a) Mexican hat wavelet and (b) its Fourier transform; a denotes scale, b is location, and f_c is the band-pass frequency attached to scale a. For the Mexican hat wavelet $f_c = \sqrt{(5/2)}/2\pi a = 0.251/a$ [e.g., see *Addison*, 2002].

energy of the signal over a range of frequencies centered around a band-pass frequency which depends on the scale a and the chosen wavelet (e.g., $f_c = 0.251/a$ for the Mexican hat wavelet used in this study). Thus the wavelet spectrum is smoother than the Fourier spectrum and for signals with frequency content which evolves over time it provides a better measure of the variance attributed to localized events of a given frequency compared to the Fourier spectrum which assumes that features of that frequency are uniformly distributed throughout the signal.

[31] Figure 9 shows a comparison of the Fourier and wavelet spectra for bed elevations recorded at probe G2 at the discharge of 2000 L s^{-1} for the gravel bed and probe S3 at the discharge of 3200 L s^{-1} for the sand bed experiment. The smoother nature of the wavelet spectrum is clearly observed allowing for a more robust estimation of the spectral slope and also a more robust identification of spectral regime transitions, as for example seen in the sand bed spectrum for very high frequencies (see Figure 9d).

[32] Figure 10 shows the wavelet spectra of gravel bed elevations measured at the location of probes G2, G3, G4, and G7 for discharges of 2000 L s^{-1} (Figure 10, left) and 2800 L s^{-1} (Figure 10, right). A clear scaling range (log-log linearity) is observed within the scales of 0.5 min to 28 min for the discharge of 2000 L s^{-1} (Figure 10, left) and 0.4 to 16 min for the discharge of 2800 L s^{-1} (Figure 10, right). In addition, the slopes of the wavelet spectrum in the scaling range, equal to approximately -1.9 and -2.1 for 2000 and 2800 L s^{-1}, respectively, are similar to those estimated in previous studies from the analysis of the Fourier spectrum of gravel bed elevation fluctuations [*Singh et al.*, 2010]. A summary of spectral slopes and scaling ranges is given in Table 2.

4.2.2. Scale-Dependent Celerity

[33] First, we consider bed form celerity determined using standard two point cross-correlation analysis. Table 3 shows the statistics obtained by standard two point cross-correlation analysis for probes G2-G6 and G4-G7 for the

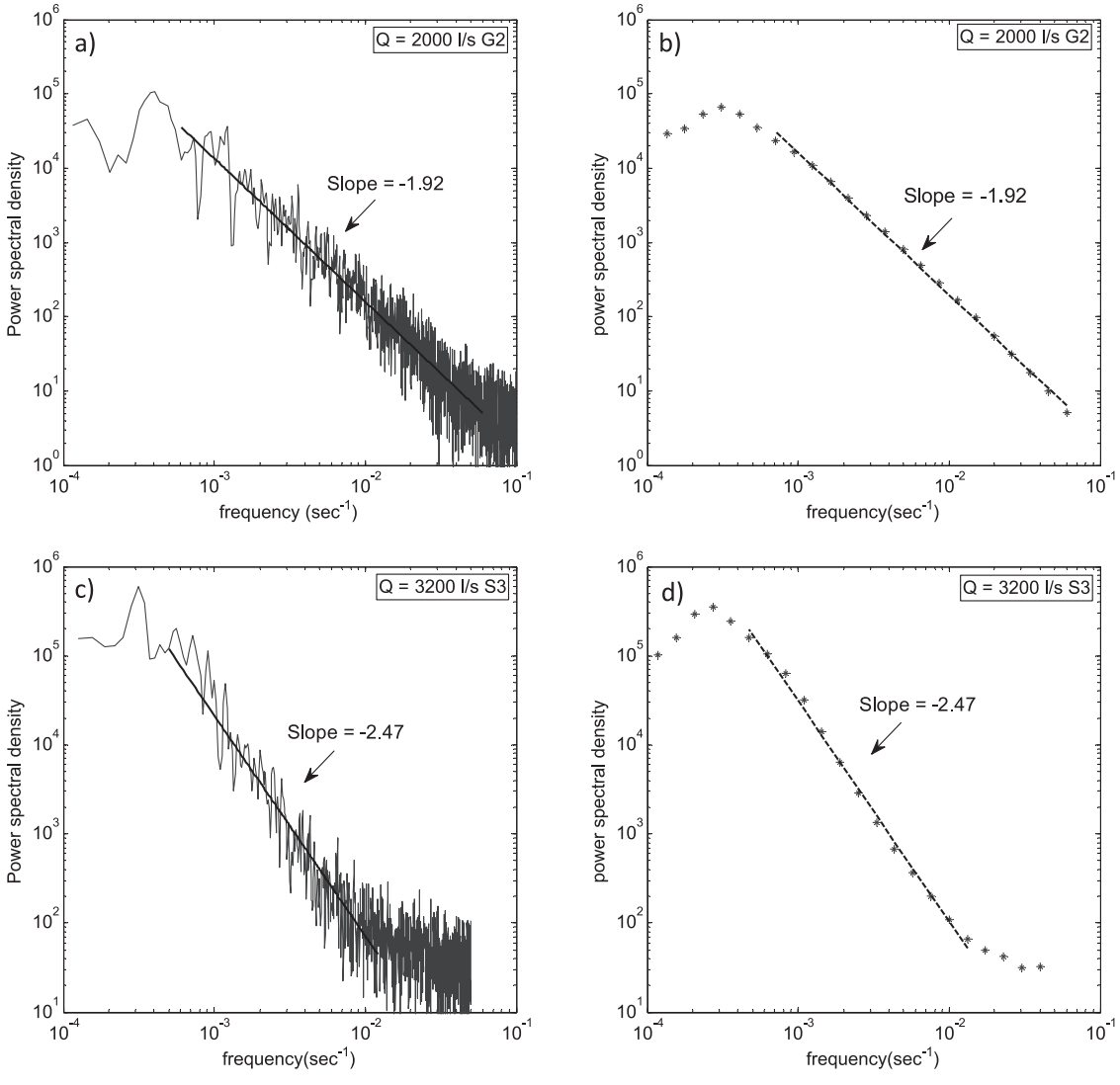

Figure 9. Comparison between (a, c) the Fourier power spectrum and (b, d) the wavelet power spectrum of bed elevation time series recorded by probe G2 in the gravel bed ($Q = 2000$ L s^{-1}, Figures 9a and 9b) and probe S3 in the sand bed ($Q = 3200$ L s^{-1}, Figures 9c and 9d) experiments.

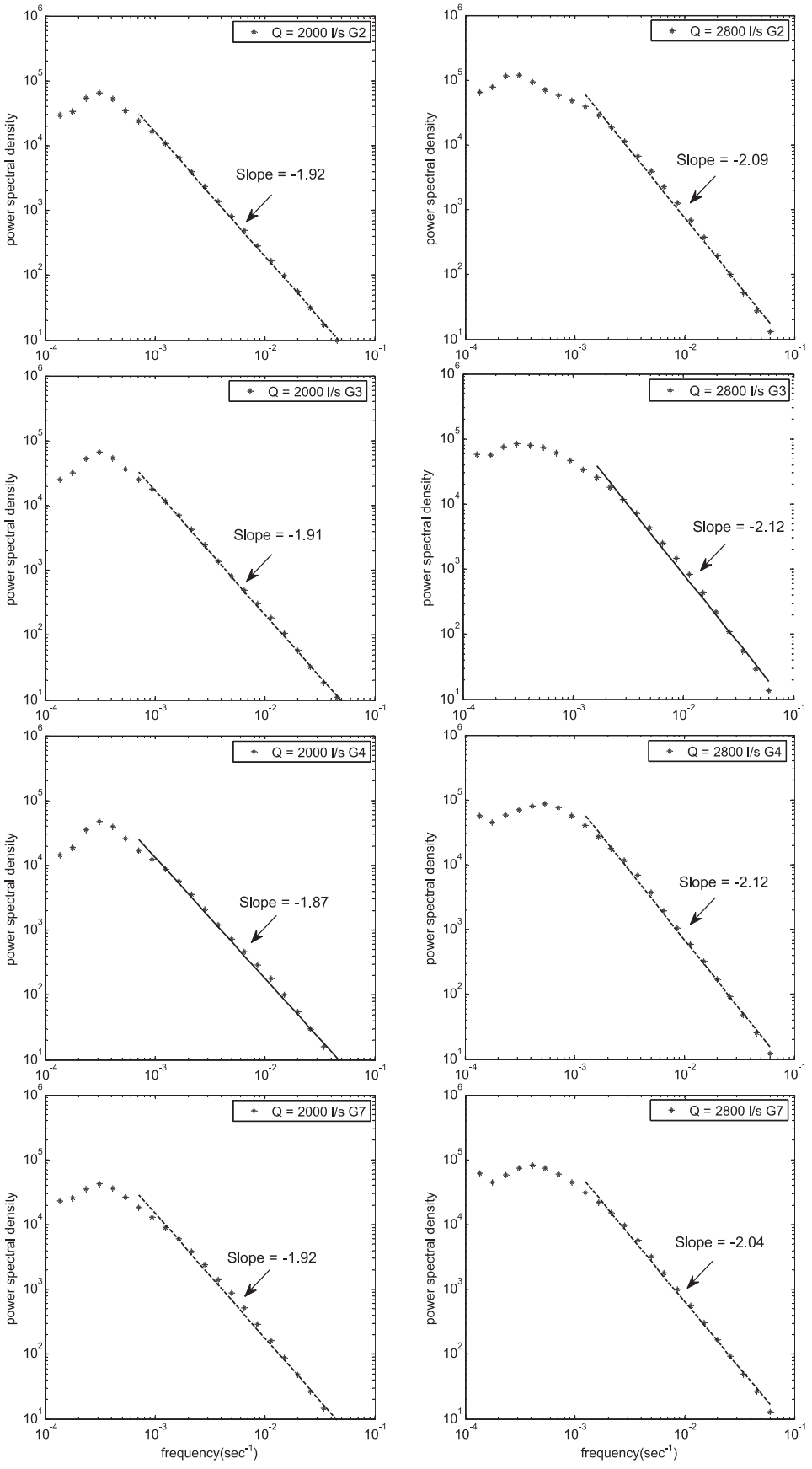

Figure 10. Wavelet spectrum of the gravel bed elevations for a discharge of (left) 2000 and (right) 2800 L s^{-1} for probes G2, G3, G4, and G7 (from top to bottom).

Table 2. Multiscale Properties of Bed Elevation Time Series

Experiment	Discharge (L s^{-1})	Probes	Spectral Slope	Spectral Scaling Range (min)	Multifractal Parameters		Structure Function Scaling Range (min)
					c_1	c_2	
Gravel	2000	G2	1.92	0.5–28	0.52	0.12	0.5–11
	2000	G3	1.91	0.5–28	0.53	0.12	0.5–10
	2000	G4	1.87	0.5–27	0.48	0.12	0.5–11
	2000	G6	1.85	0.5–28	0.50	0.12	0.5–10
	2000	G7	1.92	0.5–27	0.49	0.10	0.5–11
	2800	G2	2.09	0.4–16	0.57	0.13	0.4–7
	2800	G3	2.12	0.4–16	0.55	0.13	0.4–7
	2800	G4	2.12	0.4–16	0.59	0.12	0.4–8
	2800	G6	2.06	0.4–16	0.57	0.13	0.4–8
	2800	G7	2.04	0.4–16	0.56	0.13	0.4–8
Sand	2500	S2	2.55	2–40	0.66	0.03	1–25
	2500	S3	2.45	2–35	0.63	0.10	1–32
	2500	S4	2.93	2–41	0.68	0.04	1–30
	2500	S6	2.97	1–21	0.66	0.07	1–19
	3200	S2	2.32	2–40	0.58	0.06	1–31
	3200	S3	2.47	1–33	0.59	0.05	1–28
	3200	S4	2.78	2–24	0.66	0.06	1–19
	3200	S6	3.0	2–38	0.69	0.07	1–32

discharges of 2000 and 2800 L s^{-1}. The estimated average bed form celerities are ~14.8 m h^{-1} for 2000 L s^{-1}, and ~25.6 m h^{-1} for 2800 L s^{-1}. These values are similar to those predicted by the formula proposed by *Simons et al.* [1965] for a regular sequence of triangular bed forms, migrating without deforming:

$$q_s = \frac{(1-p)V_c h_b}{2} + q_0, \tag{9}$$

where V_c is the bed form celerity, q_s is the sediment transport rate per unit width, p is the porosity (here assumed to be 0.3), h_b is the bed form height and q_0 is a suitable integration constant, set to zero for a dune covered bed [*Simons et al.*, 1965; *Dinehart*, 2002; *McElroy and Mohrig*, 2009]. In particular, the average celerity V_c predicted by equation (9) on the basis of the sediment discharges measured at the central weighing pan and using the mean bed form height of 5 and 8.5 cm is ~15 m h^{-1} for 2000 L s^{-1} and ~28 m h^{-1} for 2800 L s^{-1}, respectively (Table 4).

[34] As discussed in section 1, various researchers have documented, both numerically and experimentally, that the celerity of bed forms is roughly inversely related to bed form height and that merging of bed forms occurs because of varying migration speeds [*Coleman and Melville*, 1994; *Schwämmle and Herrmann*, 2004; *Jerolmack and Mohrig*, 2005; *Venditti et al.*, 2005; *Giri and Shimizu*, 2006]. *Jerolmack and Mohrig* [2005] proposed a nonlinear stochastic surface evolution model to simulate bed form growth, showing that the steady state solution to the model consists of a train of bed forms. *Giri and Shimizu* [2006] used a numerical model to show that the bed form celerity decreases with increase in size of bed form geometry. These results have also been observed in laboratory and field studies [see *Venditti et al.*, 2005, and references therein].

[35] Cross-correlation analysis at multiple scales, carried out through wavelets (see section 4.1 for methodology), can provide greater insight into the dependence of bed form celerity on their size. The correlation between two multiscale processes (characterized by the presence of energy over a range of scale as shown in Figure 10) can be decomposed into correlations at multiple scales. Figure 11 shows the decomposition of bed elevation time series at scales of 2 min and 10 min for probe G4 (Figure 11, top) and probe G7 (Figure 11, bottom) for discharges of 2000 L s^{-1} (Figure 11, left) and 2800 L s^{-1} (Figure 11, right). This decomposition of the original signals via wavelets forms the basis for the computation of the scale-dependent cross-correlation coefficients. Note that these scales (2 and 10 min) are arbitrarily picked from within the scaling range of the power spectral density (see Figure 10 and Table 2). Also note that these filtered signals (wavelet coefficients) were computed using the Mexican hat wavelet and are equivalent to computing generalized second-order increments.

[36] Figures 12a and 12b show the magnitude of the maximum correlation coefficient between probes G2 and G6 and probes G4 and G7 as a function of scale for the

Table 3. Standard Cross-Correlation Statistics of Bed Elevation Series Between Different Probes

Experiment	Discharge (L s^{-1})	Probes	Distance Between Probes (m)	Maximum Correlation	Lag (s)	Bed Form Celerity (m h^{-1})
Gravel	2000	G2–G6	1.21	0.97	280	15.55
	2000	G4–G7	1.21	0.97	310	14.05
	2800	G2–G6	1.21	0.97	170	25.62
	2800	G4–G7	1.21	0.96	170	25.62
Sand	2500	S3–S6	7	0.32	1270	19.78
	3200	S3–S6	7	0.25	1860	13.51

Table 4. Bed Form Migration Celerity Obtained Using *Simons et al.*'s [1965] Relation (Equation (9))[a]

Experiment	Discharge (L s^{-1})	Pan	q_s (m^2 h^{-1})	V_c (m h^{-1})
Gravel	2000	2	0.29	16.83
	2000	3	0.25	14.44
	2000	4	0.27	15.64
	2800	2	1.06	37.85
	2800	3	0.85	28.73
	2800	4	0.99	29.91
Sand	2500	2	0.17	3.99
	2500	3	0.15	3.74
	2500	4	0.13	3.24
	3200	2	0.22	4.55
	3200	3	0.20	4.13
	3200	4	0.19	3.92

[a]Here q_s is sediment flux per unit width (m^2 h^{-1}), and V_c is bed form celerity (m h^{-1}) obtained using *Simons et al.*'s [1965] relationship. Note that for computing bed form celerity, mean bed form height was used in the relationship (see equation (9)).

discharges of 2000 and 2800 L s^{-1}, respectively. The lag corresponding to the maximum correlation, $\Delta t_{[max]}$, at each scale was computed and used for the estimation of the scale-dependent celerity. Figures 12c and 12d show the estimated bed form celerity (probes G2-G6 and G4-G7) as a function of scale for discharges of 2000 and 2800 L s^{-1}, respectively. Figure 12 suggests that the bed form celerity progressively decreases as the scale increases, i.e., larger size bed forms travel slower.

[37] A few additional observations can be made from Figure 12. First, for very small scales (say less than 5 min) the cross-correlation coefficients are very small (order of 0.1–0.5), implying either decorrelation of these small features or that linear analysis does not really capture their evolution and as a result does not allow a reliable estimate of the celerity on the basis of a cross-correlation analysis. Such small bed forms tend to be transient and are most likely to disappear or reorganize, thus preventing any correlation between the time signals measured by the two probes. For larger scales (in our case >5 min), the correlation coefficient becomes progressively larger varying in the range of $0.5 - 0.95$. Figures 12c and 12d show that the average celerity of smaller scale features is generally larger than that of larger bed forms (as expected) and that the celerity of bed forms corresponding to a time scale of the order of 10 min and larger is in close agreement to that obtained via a standard cross-correlation analysis (see Table 3). This last result is also expected as the standard cross-correlation analysis is dominated by the larger features present in the signal, ignoring thus smaller scales.

4.3. Sand Bed Topography Analysis

4.3.1. Wavelet Spectra

[38] Spectral properties of sand bed elevation series have been studied in the past both theoretically and experimentally [*Nordin and Algert*, 1966; *Hino*, 1968; *Jain and Kennedy*, 1974; *Engelund and Fredsøe*, 1982; *Nakagawa and Tsujimoto*, 1984; *Nikora et al.*, 1997; *Aberle et al.*, 2010]. In particular, it has been found theoretically, and confirmed experimentally, that the wave number spectral slope of the sand waves (computed from the spectrum of spatial bed profiles) is close to -3, in the region of large wave numbers. On the other hand, two scaling regions with slopes -3 and -2 are have been reported for the frequency spectrum (computed from time series of bed elevations), even though contrasting results exist on the range of slopes and scaling regimes where these slopes should be attained (see *Nikora et al.* [1997] for discussion).

[39] Figure 13 shows the wavelet spectra of sand bed elevations measured at the location of probes S2, S3, S4, and S6 for discharges of 2500 L s^{-1} (Figure 13, left) and 3200 L s^{-1} (Figure 13, right). In all probes, a clear scaling range (log-log linearity) is observed within the scales of approximately 2 min to 35 min, except 1 to 21 min for probe S6, at the discharge of 2500 L s^{-1}, and 2 to 24 min for probe S4 at the discharge of 3200 L s^{-1} (see Table 2 for details). The slope of the wavelet spectrum in the scaling range varies between -2.3 and -3 (see Figure 13). Although this range is larger than that observed in the gravel bed series, it is still within the range of slopes observed in other experimental and field studies [see, e.g., *Nikora et al.*, 1997, and references therein].

[40] Comparison of the gravel and sand bed spectra provides some interesting insights. First, in the gravel bed spectra the scaling regime extends all the way to the smallest scales (highest frequency) present in the signal (Figure 10). However, in the sand bed spectra there is a clear transition from one scaling regime to another or simply a break in scaling at some intermediate frequency of approximately 2 min corresponding to a wavelength of $\sim$12 cm for the discharge of 2500 L s^{-1} with an estimated speed of 3.5 m h^{-1} and $\sim$14 cm for the discharge of 3200 L s^{-1} with an estimated speed of 4 m h^{-1} (see Figure 13). *Nikora et al.* [1997] reported such a transition in scaling regime in which the higher-frequency scaling regime showed -2 spectral slope whereas the lower-frequency scaling regime showed a -3 spectral slope.

[41] A second observation from Figure 13 is that for the sand bed elevations, the wavelet spectrum does not always saturate (level off) at low frequencies (large scales) as, for example, in probes S2 and S4 for the low discharge (2500 L s^{-1}). This is indicative of the presence of very large scales perceived as nonstationarities in the limited length of the signal. These large scale features are readily apparent in the series of probes S2 and S4 at the discharge of 2500 L s^{-1} in Figure 4. Nevertheless, there is a clear scaling regime in all spectra from which reliable estimates of spectral slopes have been obtained and shown in Table 2. The transitional and three-dimensional nature of sand bed forms might be partially responsible for the wider range of spectral slopes observed in sand bed forms compared to that of the gravel bed forms.

4.3.2. Scale-Dependent Celerity

[42] Table 3 shows the statistics obtained by standard two point cross-correlation analysis between probes S3 and S6 for discharges of 2500 and 3200 L s^{-1}. The corresponding average bed form celerities are $\sim$20 and $\sim$13.5 m h^{-1}, respectively. These values are much larger than those estimated through equation (9) on the basis of mean bed form height and mean sediment transport rate and also by considering the number of bed form units present in the time sequence (see Table 4). For example, assuming that 12 bed forms (see Figure 6j) are sampled in about 540 min with an

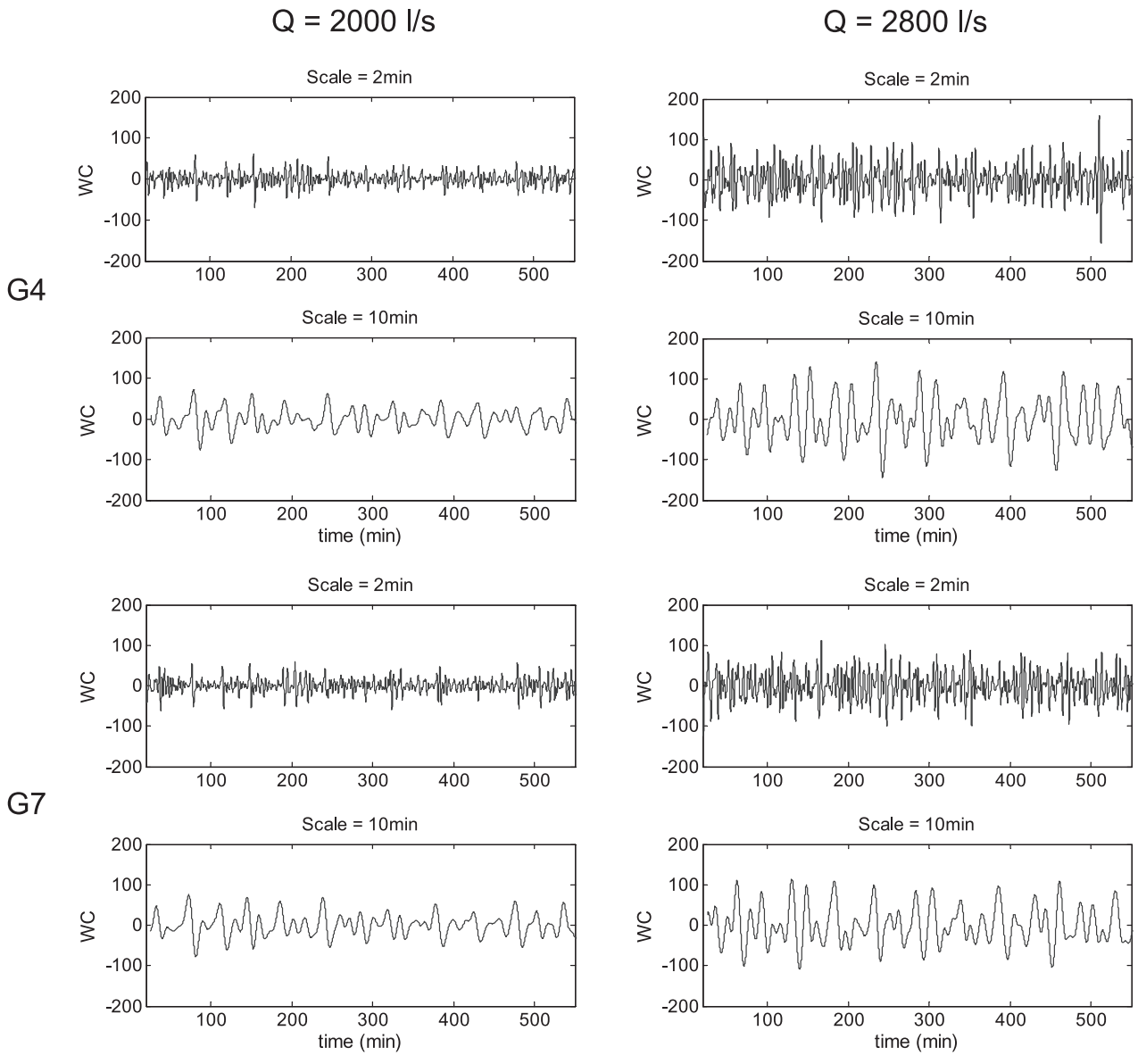

Figure 11. Wavelet coefficients of the gravel bed elevation series computed using the Mexican hat wavelet at scales of 2 and 10 min for the discharges of (left) 2000 and (right) 2800 L s^{-1}. (top) Probe G4 and (bottom) probe G7.

average wavelength of about 4 m, implies a bed form period of about 45 min (0.75 h). The corresponding celerity is approximately 5 m h^{-1}, quite close to the mean value of 4.2 m h^{-1} predicted by equation (9). This inability of cross correlation to estimate correctly bed form celerity is related to the relatively large distance (7 m) between probes S3 and S6 (see Figure 14). Clearly, cross-correlation analysis cannot capture the evolution of bed forms much smaller than this distance. Moreover, the distance between probes is also too large to give reliable information on the migration of even the largest dunes, which were observed to undergo significative deformations as they move downstream. These deformations are responsible for the low correlation coefficients (of the order of 0.4–0.5 for the largest scales) compared to the corresponding 0.9 correlation coefficient observed in the gravel bed experiments (see Figure 12). Unfortunately cost and logistics precluded us from repeating these sand experiments, an issue that we plan to address in future.

5. Scale-Dependent Statistics of Bed Elevation Increments

5.1. Higher-Order Structure Function Analysis

[43] In order to investigate the multiscale structure of the bed elevation series $h(t)$ over a range of scales, a higher-order statistical analysis can be performed on the bed elevation series. For that purpose, one can use the wavelet coefficients at different scales as computed earlier via the Mexican hat wavelet, or simply use the bed elevation increments, $\Delta h(t, a)$ defined as

$$\Delta h(t, a) = h(t + a) - h(t), \tag{10}$$

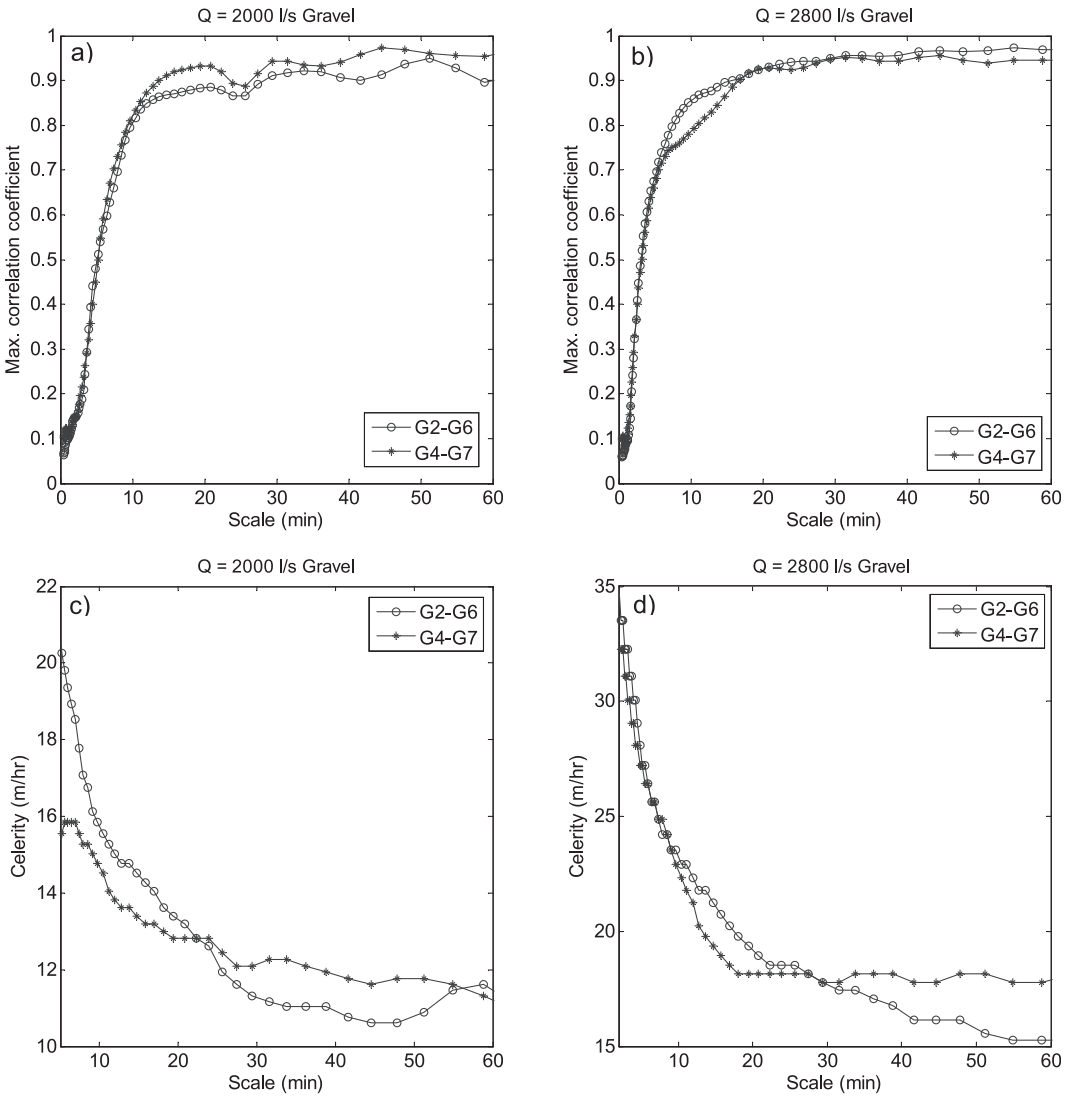

Figure 12. Plot of maximum cross correlation obtained between probes G2 and G6 and G4 and G7 for a discharge of (a) 2000 and (b) 2800 L s^{-1} as a function of scale using wavelet analysis. Celerity of bed forms as a function of scale for a discharge of (c) 2000 and (d) 2800 L s^{-1}. Note that the lag used in computing celerity at a given scale corresponds to the maximum cross-correlation coefficient obtained between probes G2-G6 and G4-G7 at that scale.

where t is the time and a is the scale. Notice that while $h(t)$ can only be positive (since $h(t)$ is computed with reference to the lowest bed elevation i.e., the global minimum), the increments $\Delta h(t,a)$ can be both positive and negative, and in fact they have a zero mean. Using first-order increments defined as above is equivalent to using the simplest wavelet (Haar wavelet) and it is warranted to remove piecewise constant trends from the series. We note that we have performed the analysis using different wavelets with no appreciable difference on the results, so we resort here to reporting the results of the first-order increment analysis as also done by *Nikora and Goring* [2001] and *Nikora and Walsh* [2004].

[44] The estimates of the qth-order statistical moments of the absolute values of the increments at scale a, also called the partition functions or structure functions $M(q,a)$, are defined as

$$M(q,a) = \frac{1}{N}\sum_{t=1}^{N} |\Delta h(t,a)|^q, \tag{11}$$

where N is the number of data points of the series at scale a. The statistical moments $M(q,a)$ for all q completely describe the shape of the probability density function (pdf) of the increments at scale a. Statistical scaling, or scale invariance, requires that $M(q,a)$ is a power law function of the scale, that is,

$$M(q,a) \sim a^{\tau(q)}, \tag{12}$$

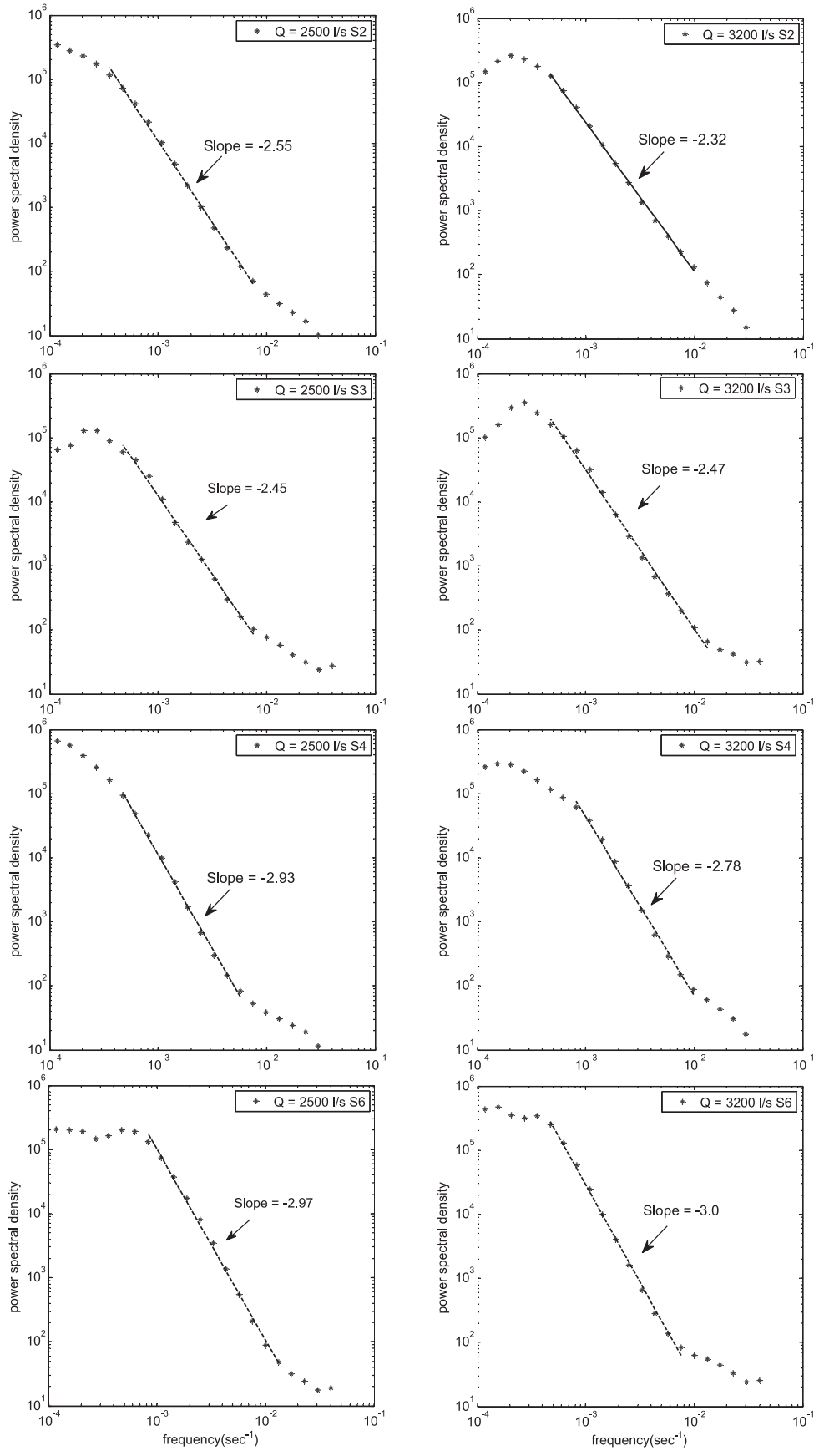

Figure 13. Wavelet spectrum of the sand bed elevations for a discharge of (left) 2500 and (right) 3200 L s^{-1} for probes S2, S3, S4, and S6 (from top to bottom).

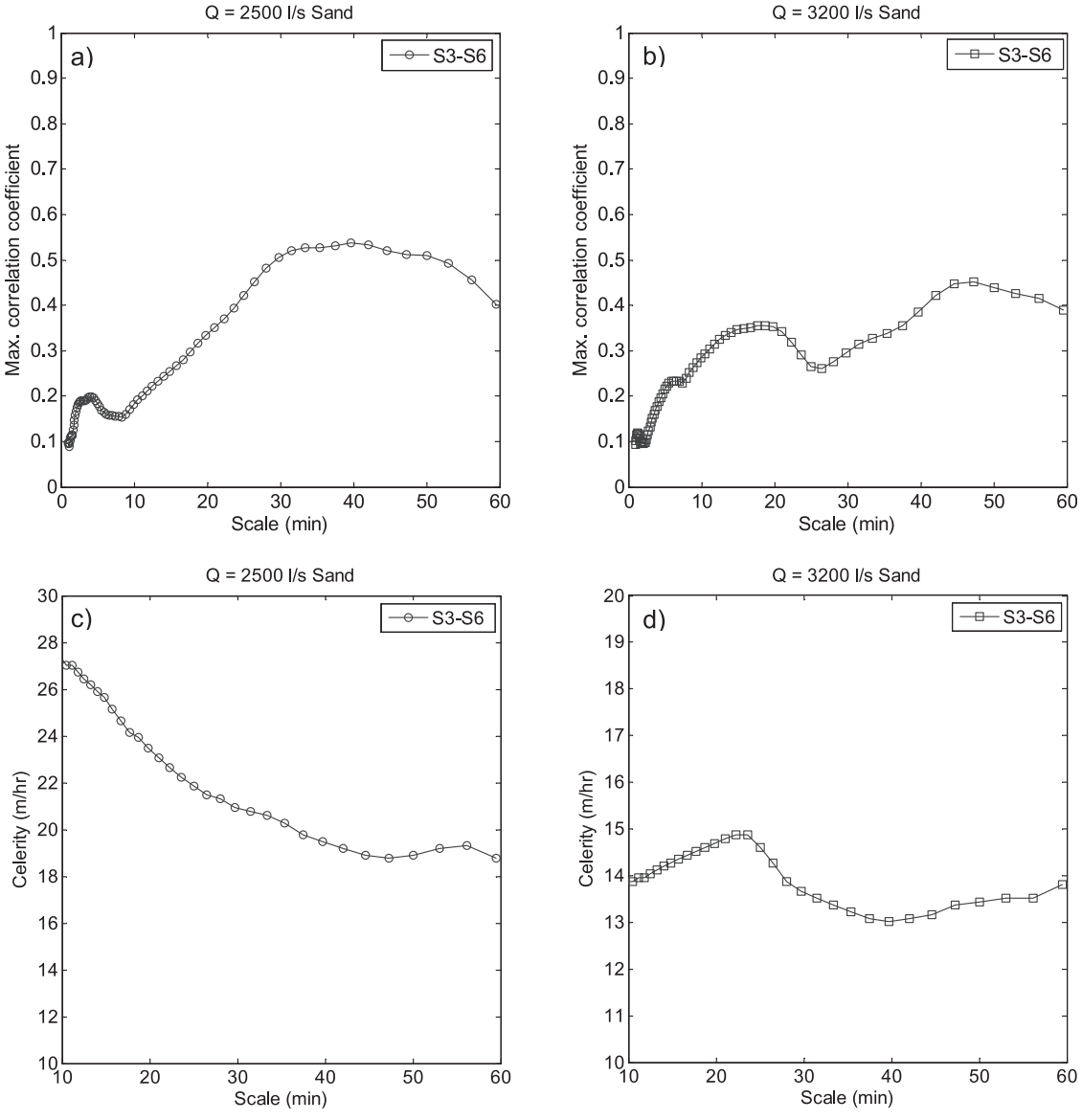

Figure 14. Plot of maximum cross correlation obtained between probes S3 and S6 for a discharge of (a) 2500 and (b) 3200 L s^{-1} as a function of scale using wavelet analysis. Celerity of bed forms as a function of scale for a discharge of (c) 2500 and (d) 3200 L s^{-1}. Note that the lag used in computing celerity at a given scale corresponds to the maximum cross-correlation coefficient obtained between probes S3 and S6 at that scale.

where $\tau(q)$ is the so-called scaling exponent function. Therefore, for a scale-invariant series, the function $\tau(q)$ completely determines how the pdf of the increments changes with scale [e.g., *Castaing et al.*, 1990; *Venugopal et al.*, 2006; *Singh et al.*, 2009a]. The simplest form of scaling, known as simple scaling or monoscaling, is when the scaling exponents are a linear function of the moment order, i.e., when $\tau(q) = Hq$. If $\tau(q)$ is nonlinear, the process is called multiscaling and more than one parameter is required to describe the evolution of the pdfs over scales [e.g., *Castaing et al.*, 1990; *Venugopal et al.*, 2006]. For most processes the nonlinear relationship describing $\tau(q)$ with q can be parameterized as a polynomial, and the simplest form is a quadratic approximation:

$$\tau(q) = c_1 q - \frac{c_2}{2} q^2. \tag{13}$$

[45] The multiscale analysis in this framework provides a compact way, using two parameters c_1 and c_2, of parameterizing the change of the pdf over a range of scales. The parameter c_1 is a measure of the average "roughness" of the series (akin to the Hurst exponent H) and c_2 is the so-called intermittency parameter. A value of c_2 different than zero implies that the tails of the distribution stretch differently than the body as one changes scale. Following the geometrical interpretation of the statistical scaling [e.g., *Frisch*, 1995; see also *Venugopal et al.*, 2006], the parameter c_2 relates to the local roughness or degree of differentiability of the signal, as measured by the local Hölder exponent. A value of $c_2 \neq 0$ implies a temporally nonstationary or spatially inhomogeneous arrangement of spikes and thus the presence of a distribution of local Hölder exponents as opposed to a single value of H for a simple scaling process. In other words, the signal contains pockets

of high fluctuations arranged over its domain in such a way that they manifest statistically in complicated ways.

[46] Structure function analysis as described above was performed on the bed elevation time series shown in Figures 3 and 4. Figures 15 (top) and 16 (top) show the scaling of the moments of the bed elevation increments $\Delta h(t, a)$ as a function of scale a for gravel bed experiments (probe G3, discharges of 2000 L s^{-1} and 2800 L s^{-1}), and sand bed experiments (probe S3, discharges of 2500 and 3200 L s^{-1}). Note that these plotted moments are offset vertically (along the y axis) for better visualization. For the gravel bed experiment, the structure functions follow power law scaling over a range of 0.5 to 10 min for the discharge of 2000 L s^{-1} and 0.4 to 7 min for the discharge of 2800 L s^{-1}. For the sand bed experiment, the structure functions follow a power law relation with scale a, over a range of scales from 1 to 32 min and 1 to 28 min for the discharge of 2500 L s^{-1} and 3200 L s^{-1}, respectively (see Figure 16). A summary of scaling ranges for the other probe locations at different discharges for both gravel and sand bed experiments can be seen in Table 2.

[47] Figures 15 (bottom) and 16 (bottom) show the computed $\tau(q)$ curves from the slopes of the moments shown in Figures 15 (top) and 16 (top) within the scaling range, respectively. We see that the $\tau(q)$ curves have a nonlinear dependence on q, indicating the presence of multifractality for both gravel and sand bed experiments for all the discharges. The parameters of multifractality (for all locations and discharges considered in the previous analysis) were calculated by approximating the $\tau(q)$ as a quadratic function in q and are shown in Table 2. Note that for brevity we have plotted the structure functions and the $\tau(q)$ curve for probes G3 and S3 only for both the discharges and bed configuration; however the multifractality parameters c_1 and c_2 of the other probes (probes G2, G3, G4, G6, and G7 for gravel bed experiments and probe S2, S3, S4, and S6 for sand bed experiments for all the discharges considered in this study) are reported in Table 2 along with their scaling range.

[48] Several observations can be made from the multifractal properties of the bed elevations shown in Table 2 for gravel and sand bed experiments. In general, the intermittency parameter, c_2, is larger in the case of gravel bed

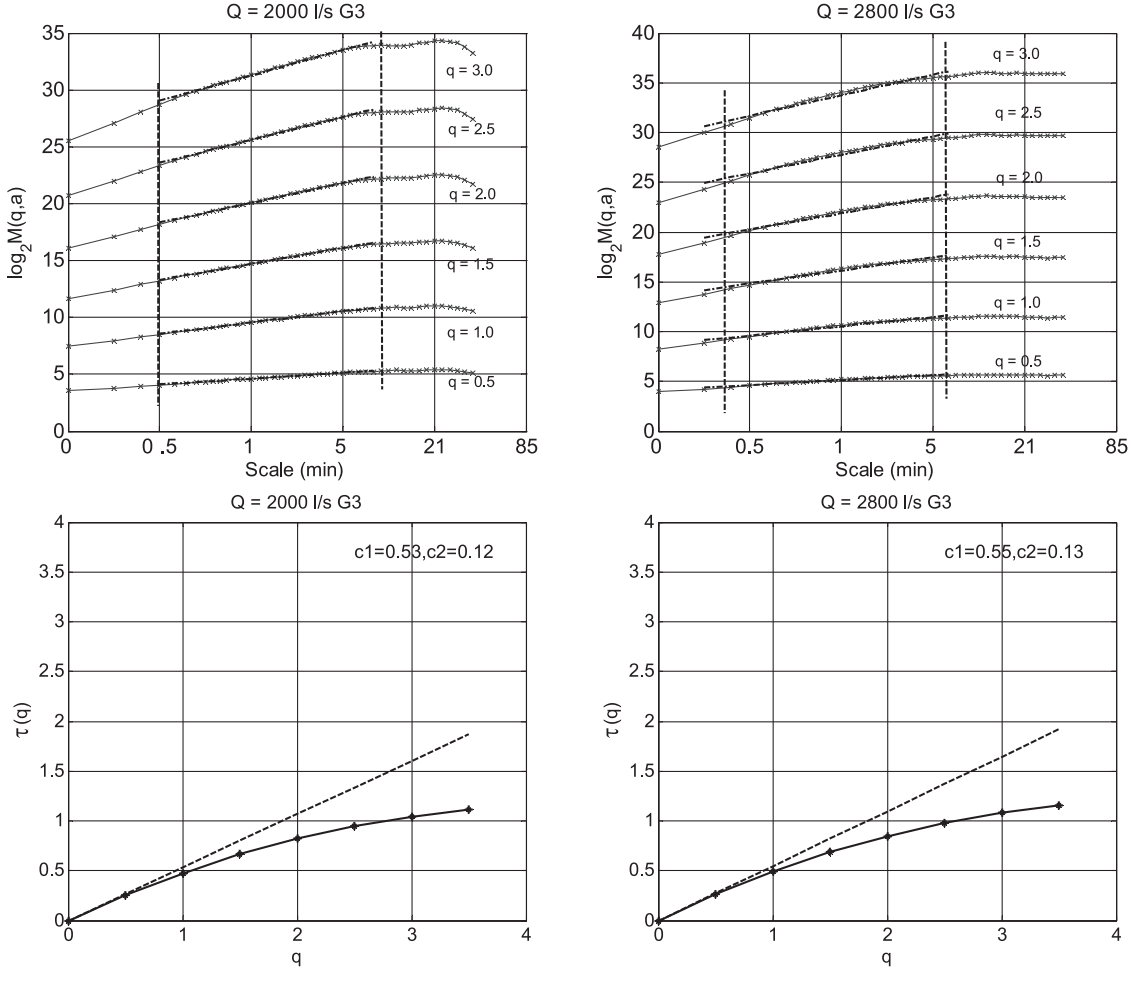

Figure 15. (top) Statistical moments of the gravel bed elevation increments as a function of scale and (bottom) the scaling exponents $\tau(q)$ estimated from the log-log linear regressions within the scaling regimes for discharges of (left) 2000 and (right) 2800 L s^{-1}. Note the deviation of $\tau(q)$ from the linear line, establishing the presence of multifractality.

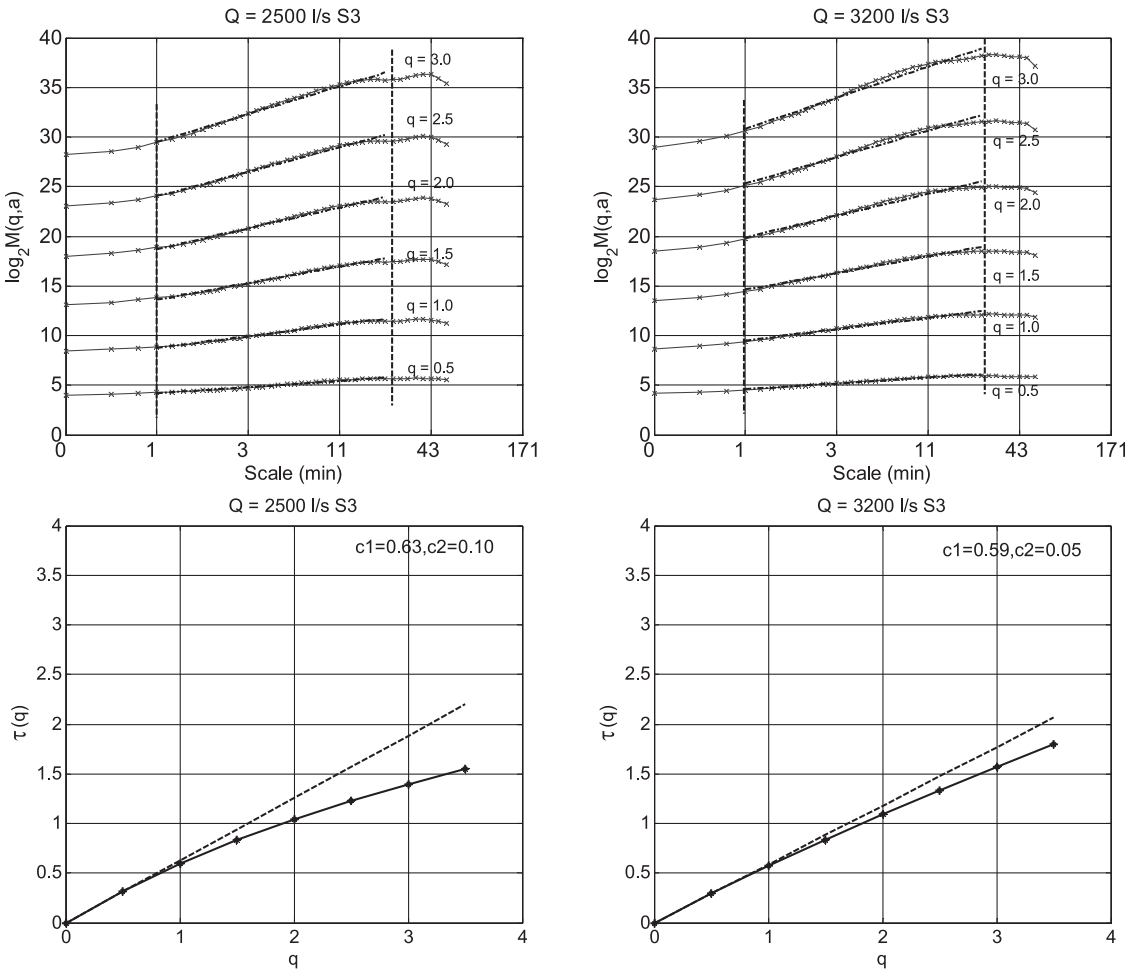

Figure 16. (top) Statistical moments of the sand bed elevation increments as a function of scale and (bottom) the scaling exponents $\tau(q)$ estimated from the log-log linear regressions within the scaling regimes for discharges of (left) 2500 and (right) 3200 L s^{-1}. Note the deviation of $\tau(q)$ from the linear line, establishing the presence of multifractality.

elevation than sand bed elevation, suggesting a more inhomogeneous arrangement of the various strength singularities or abrupt bed elevation fluctuations over time in the gravel bed compared to the sand bed. This is consistent with the presence of sorting waves and grain clusters present at scales between the grains and the dunes. On the other hand, the roughness parameter c_1 is smaller in the case of gravel bed experiments than sand bed experiments, suggesting that sand bed elevation fluctuations are smoother than gravel bed elevation fluctuations. Also, in comparing the scaling range of structure functions (see Table 2 for scaling ranges), the scaling range is much smaller in the case of gravel bed (of the order of 1–10 min, on an average) than the scaling range in the sand bed (of the order of 1–30 min, on an average) experiments.

5.2. The pdf of Bed Elevation Increments as a Function of Scale

[49] Most studies to date have concentrated on characterizing the pdf of mean-removed bed elevations, often referred to as "fluctuations around the mean." Mean-removed bed elevations in plain beds, for which the mean bed elevation can be meaningfully defined, have been reported to be approximately Gaussian [e.g., *Wong et al.*, 2007]. However, in the presence of bed forms, bed elevation increments rather than "fluctuations around the mean" are more meaningful for statistical analysis as differencing removes nonstationarities (due to bed forms), rendering the increment series stationary and amenable to statistical analysis. (Note that, following the turbulence terminology, the increments as defined in equation (10) were called "fluctuations" by *Singh et al.* [2009a]. Here we will use the terms "increments" and "fluctuations" interchangeably and in contrast to the "fluctuations around the mean.") To the best of our knowledge, the pdf's of gravel and sand bed elevation increments have not been explicitly reported before although their statistical moments have been characterized via structure function analysis [e.g., *Nikora et al.*, 1997, 1998; *Marion et al.*, 2003; *Nikora and Goring*, 2001; *Nikora and Walsh*, 2004; *Aberle and Nikora*, 2006; *Singh et al.*, 2009a].

[50] Figure 17 shows the semilog pdf's of the bed elevation increments for the gravel bed (Figures 17a and 17b) and sand bed (Figures 17c and 17d) elevations. These pdf's

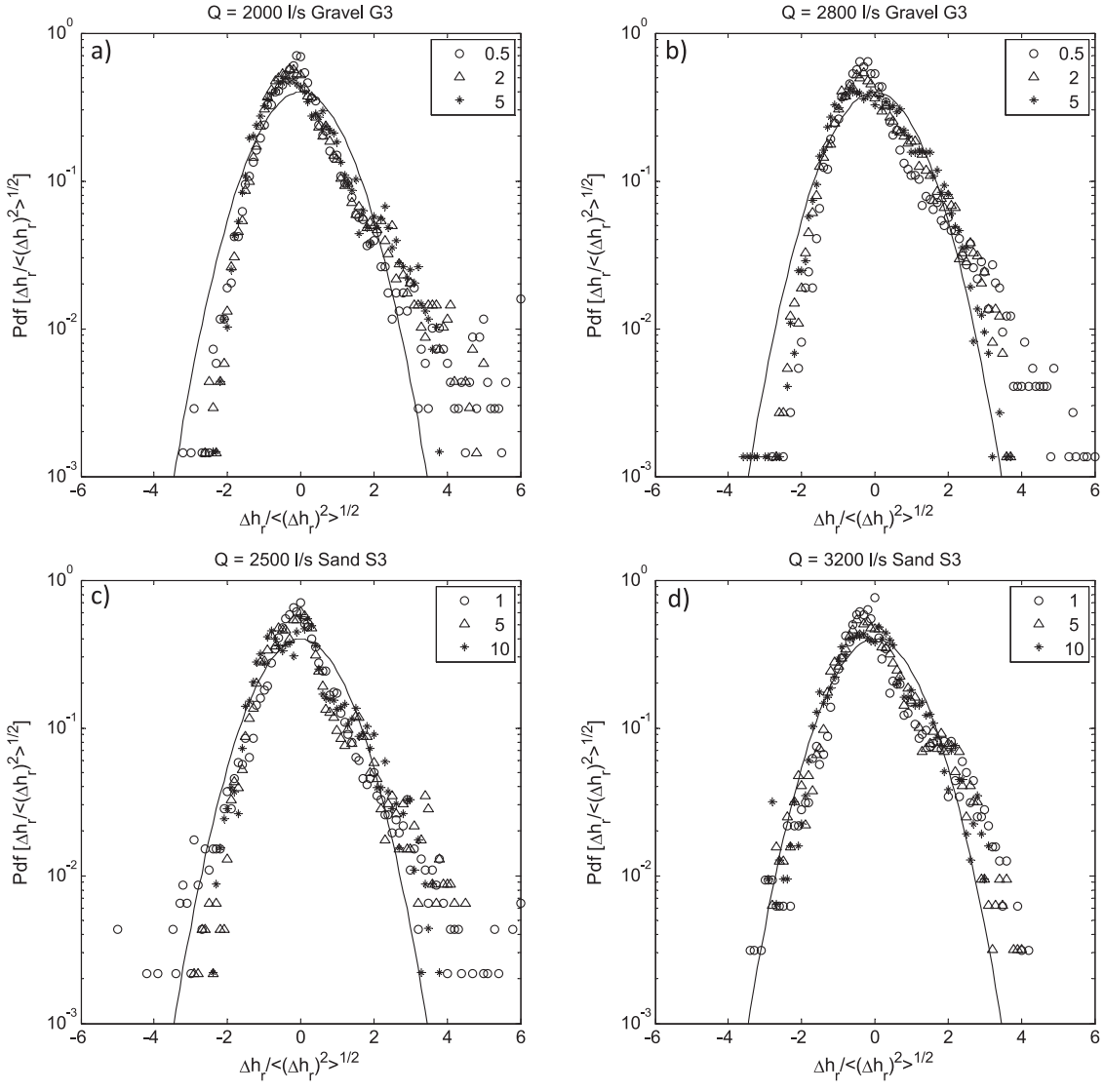

Figure 17. Semilog pdf's of the normalized increments ($\Delta h_r = h(t+r) - h(t)$) of the bed elevation measured at the location of probe G3 for the gravel bed experiments (Figures 17a and 17b) and probe S3 for the sand bed experiments (Figures 17c and 17d) for a discharge of (a) 2000, (b) 2800, (c) 2500, and (d) 3200 L s^{-1}. For the gravel bed experiments (Figures 17a and 17b), circles correspond to a time lag $r = 0.5$ min, triangles correspond to $r = 2$ min, and stars correspond to $r = 5$ min, while for the sand bed experiments (Figures 17c and 17d), circles correspond to $r = 1$ min, triangles correspond to $r = 5$ min, and stars correspond to $r = 10$ min. The solid curve designates the Gaussian distribution.

were computed from the bed elevation recorded by probe G3 for discharges of 2000 L s^{-1} (Figure 17a) and 2800 L s^{-1} (Figure 17b) and by probe S3 for discharges of 2500 L s^{-1} (Figure 17c), and 3200 L s^{-1} (Figure 17d). Similar pdf's have been obtained from the bed elevation sampled at other probe locations and for brevity are not shown here. The pdf's were computed at the scales of 0.5 min, 2 min, and 5 min for the gravel bed experiments and 1 min, 5 min, and 10 min for the sand bed experiments. These scales were arbitrarily chosen from within the scaling range obtained from the structure function analysis of bed elevations (see Table 2 and discussion in the next few paragraphs). It is observed that the pdf's at all scales have heavier tails than a Gaussian pdf (solid line in Figure 17). However, on close inspection one can see that the pdf's of bed elevation increments tend to become thinner tailed at larger scales, as can be seen more clearly from Figure 18, which shows the log-log plots of the probability of exceedance of the positive bed elevation increments ($\Delta h(t) > 0$) measured through probe G3 (Figures 18a and 18b) and probe S3 (Figures 18c and 18d) for a discharge of 2000 L s^{-1} (Figure 18a) and 2800 L s^{-1} (Figure 18b) for the gravel and 2500 L s^{-1} (Figure 18c) and 3200 L s^{-1} (Figure 18d) for the sand bed experiments. This behavior is similar to that experienced by turbulent velocity fluctuations: at smaller scales (close to Kolmogorov scale) the pdf's of the velocity fluctuations are stretched

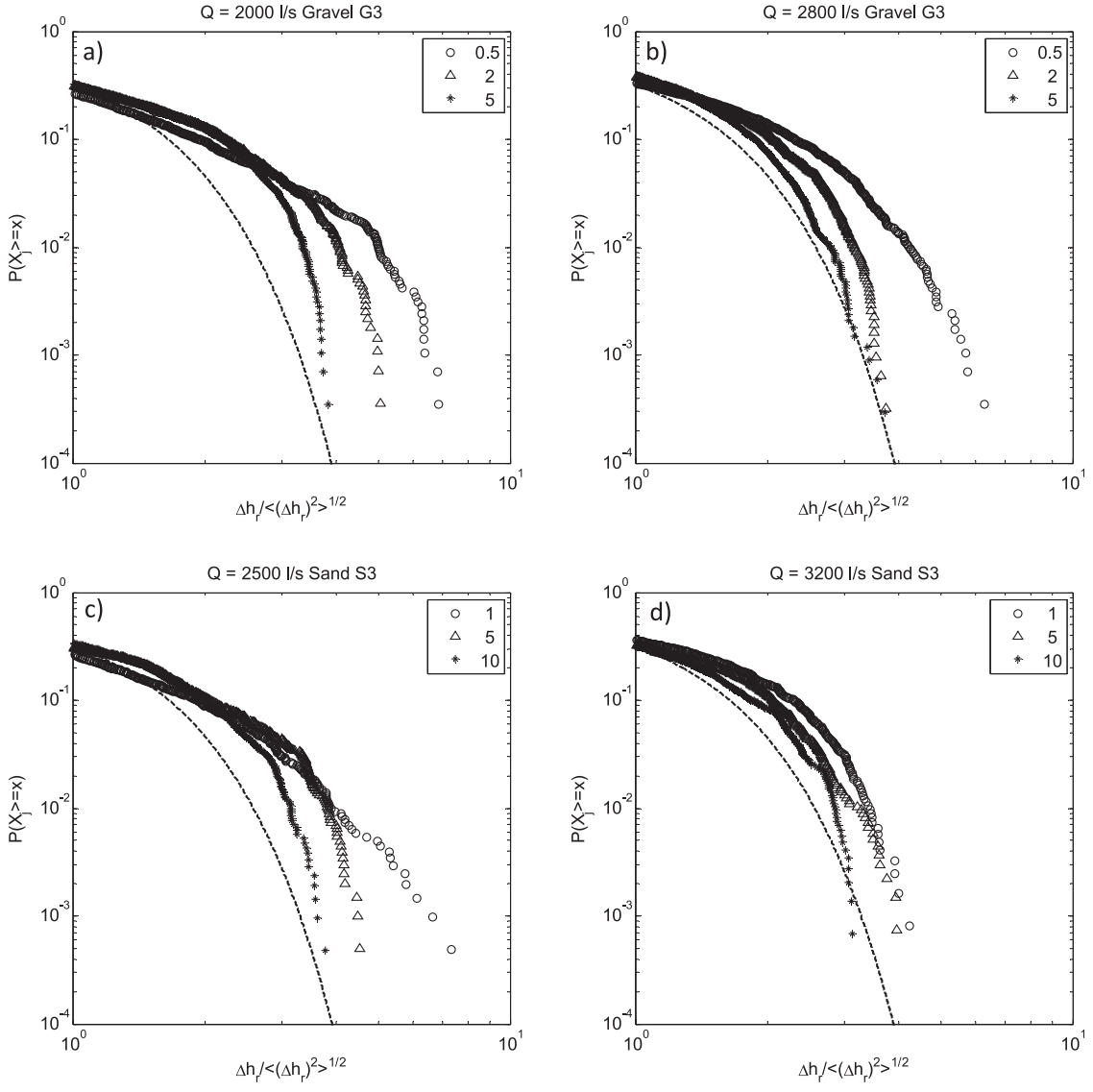

Figure 18. Log-log exceedance probabilities of the normalized positive increments of the bed elevation measured at the location of probe G3 for the gravel bed experiments (Figures 18a and 18b) and probe S3 for the sand bed experiments (Figures 18c and 18d) for a discharge of (a) 2000 L s^{-1}, (b) 2800, (c) 2500, and (d) 3200 L s^{-1}. For the gravel bed experiments (Figures 18a and 18b), circles correspond to a time lag $r = 0.5$ min, triangles correspond to $r = 2$ min, and stars correspond to $r = 5$ min, while for the sand bed experiments (Figures 18c and 18d), circles correspond to $r = 1$ min, triangles correspond to $r = 5$ min, and stars correspond to $r = 10$ min. The dashed curve designates the Gaussian distribution.

exponential, whereas they tend to become Gaussian at larger scales (close to the integral scale) [e.g., *Frisch*, 1995; *Malecot et al.*, 2000].

[51] It is important to note that the structure function analysis as described in section 5.1, i.e., using the absolute value of increments, characterizes the change in the shape of symmetric pdf's as a function of scale [see also *Frisch*, 1995; *Malecot et al.*, 2000; *Venugopal et al.*, 2006]. However here we note the asymmetric nature of the pdf's of bed elevation increments (see Figure 17). Possibly, a separate investigation of the positive and negative sides of the pdf of bed elevation increments as a function of scale and how these might relate to the physics of bed form dynamics in the lee and the stoss side of the bed forms is warranted to provide more insight. This will be the subject of a future study.

6. Nonlinearity and Complexity in Bed Form Dynamics

[52] Many natural systems, although deterministic, exhibit a limited degree of predictability because of complex nonlinear dynamics which amplify small perturbations and lead to chaotic behavior [e.g., *Lorenz*, 1969]. Simply put, two points infinitesimally close to each other grow apart as

the system evolves and the rate of exponential growth of their trajectories can be used as a measure of the nonlinear complexity or lack of predictability in the system. Let us consider the bed elevations $h(t)$ as a dynamical system with an evolution law given by the differential equation

$$\frac{dh}{dt} = F(h) \tag{14}$$

or in the case of discrete time by

$$h(t+1) = G[h(t)]. \tag{15}$$

Note that the state of the system $h(t)$ can be replaced by a vector $\mathbf{h}(t)$, i.e., be augmented to include elevations at previous times, such that $\mathbf{h}(t)$ uniquely specifies the state of the system. (Here we will denote the state of the system simply as $h(t)$). Nonlinear dynamical system analysis studies the separation between two trajectories $h(t)$ and $h'(t)$ starting from two close initial conditions $h(0)$ and $h'(0) = h(0) + \delta h(0)$, respectively. As long as the difference between the trajectories, $\delta h(t) = h'(t) - h(t)$ remains small (strictly speaking infinitesimal), a standard indicator of the behavior of such a dynamical system with respect to the asymptotic evolution of an infinitesimal perturbation is the maximum Lyapunov exponent $\lambda_{\max}$, i.e.,

$$|\delta h(t)| \sim |\delta h(0)| e^{\lambda_{\max} t}. \tag{16}$$

That is, if $\lambda_{\max} > 0$ one has a rapid (exponential) amplification of an error on the initial condition. In such a case, the system is chaotic and unpredictable at long times. Indeed, if we put $\delta = |\delta h(0)|$ for an initial error and want to predict the state of the system with a certain tolerance Δ, the prediction is possible only up to a predictability time given by

$$T_p \sim \frac{1}{\lambda_{\max}} \ln \frac{\Delta}{\delta}. \tag{17}$$

This equation shows that T_p is basically determined by the maximum Lyapunov exponent since its dependence on δ and Δ is very weak. It is emphasized that the above formula holds only for infinitesimal perturbations, and, by construction, it cannot assess the predictability in systems with many scales of variability, such as turbulence or bed elevation fluctuations, which possess a hierarchy of scales. In those multiscale systems the predictability time T_p is determined by the nonlinear mechanism responsible for the error growth of finite size perturbations. To address these issues, *Aurell et al.* [1996] proposed a generalization of the maximum Lyapunov exponent method. Specifically, they introduced the quantity $T_p(\delta, \Delta)$ which is the time it takes for a finite perturbation to grow from an initial size δ (in general not infinitesimal) to a tolerance level Δ. The so-called finite size Lyapunov exponent (FSLE) $\lambda(\delta)$ is then the average of some function of this error growing time n_r (time for a perturbation of initial size δ to grow to a size $\delta(n_r)$):

$$\lambda(\delta) = \left\langle \frac{1}{n_r} \right\rangle \ln \left[\frac{\delta(n_r)}{\delta} \right]. \tag{18}$$

In this case the average predictability time can be written as

$$T_p(\delta, \Delta) = \int_{\delta}^{\Delta} \frac{d\ln\delta'}{\lambda(\delta')}. \tag{19}$$

[53] Various methodologies are available for computing finite size Lyapunov exponents [see *Aurell et al.*, 1997]. In the present contribution we have adopted the method of *Boffetta et al.* [1998, 2002; see also *Basu et al.*, 2002; *Singh et al.*, 2009b]. There are two parameters that need to be determined for the computation of the FSLE. These are the delay time (d) and the embedding dimension (e). The delay time ensures the removal of linear auto correlation in the series by considering values that are further than the decorrelation distance. The embedding dimension is the dimension of the space where the times series is projected for assessing the evolution of the trajectories of nearby "points" in that projection space (called the phase space) as time evolves. The delay time d and embedding dimension e adopted in this analysis of the bed elevation series for both discharges and materials (gravel and sand) were chosen to be $d = 10$ and $e = 3$ following the mutual information and false nearest-neighbor approaches, respectively [see *Kantz and Schreiber*, 1997; *Singh et al.*, 2009b]. The estimation of d and e and the computation of the FSLE were performed using the TISEAN package [*Hegger et al.*, 1999], a set of algorithms available online for analyzing nonlinear time series which includes data representation, prediction, noise reduction, dimension and Lyapunov exponent estimation, and nonlinearity testing [*Hegger et al.*, 1999].

[54] Figure 19 shows the predictability time T_p (in seconds) computed using the FSLE methodology as a function of the tolerance level Δ in mm for the discharges of 2000 and 2800 L s^{-1} at the location of G3 for gravel bed (Figure 19a) and for the discharge 2500 and 3200 L s^{-1} at the location of S3 for sand bed (Figure 19b) experiments. The initial error δ was specified to be $\sim d_{50}$, i.e., 8 mm for the gravel bed and 1 mm for the sand bed. As expected, the predictability time, i.e., the time interval over which one can typically forecast the system, is longer for the slower moving bed forms (smaller discharge rates) than for the faster moving bed forms (higher discharge rates); note that the curves for lower discharge are above the corresponding high discharge curves.

[55] Moreover, this predictability time increases approximately as a power law with the tolerance level Δ, that is,

$$T_p \sim \Delta^{\gamma}, \tag{20}$$

where $\gamma \sim 1.9$ to 2.1 for gravel and $\gamma \sim 1.25$ to 1.5 for sand. This indicates that, for example, doubling the tolerance level Δ increases the rate of predictability by a factor of approximately 2^2 in gravel bed versus $2^{1.4}$ in sand bed, suggesting that the gravel bed elevation dynamics are, in general, more predictable compared to the sand bed dynamics. This result from nonlinear dynamics analysis point of view is consistent with the results obtained from the linear analysis performed earlier which indicated a more three-dimensional structure and higher deformation rates of the sand bed forms compared to the gravel bed forms. Also,

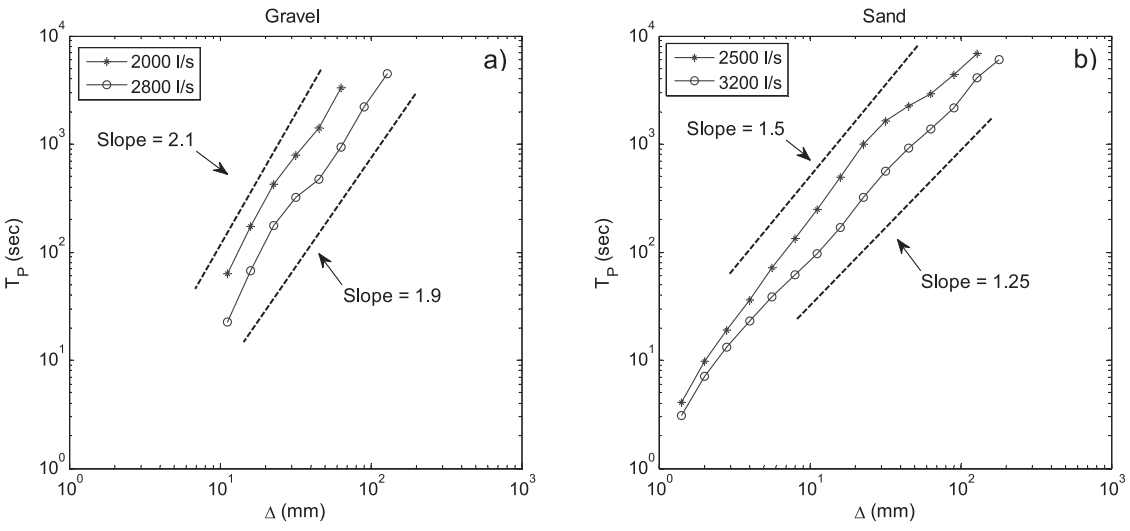

Figure 19. Predictability time T_p, based on finite size Lyapunov exponent, as a function of prediction error tolerance Δ for bed elevation sampled (a) at the location of probe G3 for a discharge of 2000 and 2800 L s^{-1} for gravel bed experiments and (b) at the location of probe S3 for a discharge of 2500 and 3200 L s^{-1} for gravel bed experiments. The initial perturbation was specified to be d_{50}, i.e., 8 mm for the gravel bed and 1 mm for the sand bed. See text for more explanation.

slower increase of the predictability time for a given rate of tolerance level Δ increase (smaller slope γ) for the case of higher discharges (for both gravel and sand bed configuration), possibly quantifies the fact that higher discharge introduces more complex bed features enhancing nonlinearity and complexity on the bed topography.

[56] Overall, this data-based nonlinear analysis suggests that the information provided by the predictability time estimated through FSLE can be used to objectively quantify the complex behavior of a migrating bed and, therefore, to develop metrics for assessing the performance of mechanistic models of sediment transport and estimate upper limits of prediction time by any model.

7. Summary and Concluding Remarks

[57] Knowledge of the dynamics of migrating bed forms is essential for characterizing sediment transport in alluvial rivers or in channels whose bed consists of self-organized bed forms of different sizes and geometries. These bed forms exhibit complex dynamics affected by the multiscale interaction of near-bed turbulence, particle-to-particle interactions, and the stochastic nature of entrainment and deposition. Bed elevations can now be easily measured with acoustic probes, as can turbulent velocity fluctuations in the flow. This technology introduces the opportunity to perform advanced statistical analysis of the flow, transport, and bed configuration. In a previous publication [*Singh et al.*, 2010], we demonstrated how the time scales of moving bed forms can be estimated from the spectra of the near-bed turbulent velocity fluctuations on the basis of the presence of a spectral gap between an energy production regime due to migrating bed topography and the inertial subrange regime of turbulence. Here we focus on multiscale measures for characterizing the complex nature of bed form migration. Our goal is to provide objective methodologies for comparing bed forms, such that inferences can be made beyond average quantities (e.g., mean bed form height, length, and celerity), hypotheses can be tested, and guidance for further physical understanding and model development can be provided.

[58] Our analysis is based on a multiscale statistical study of bed form evolution in a laboratory flume. Different water discharges were used to transport sediment and create bed forms in sand and gravel in a large-scale experimental channel at the St. Anthony Falls Laboratory of University of Minnesota. The primary data used in the analysis are time series of bed elevations recorded with acoustic probes at different locations within the channel as well as a continuous record of sediment transport at the downstream end of the flume.

[59] A simple filtering and thresholding methodology is introduced to estimate bed form height. Interestingly, the probability distribution of bed form height has a similar shape for both gravel or sand substrates and its positive tail is slightly thicker than Gaussian. Both gravel and sand bed elevation series exhibit a multiscale structure, i.e., the presence of features of multiples scales, which manifests itself in a power law spectrum within a scaling range. The spectral signature of bed elevation of evolving bed forms is of theoretical and practical interest and has been explored before in the literature via modeling experimental and field observations. Wavelet analysis of the bed elevation series produces much smoother spectra than Fourier analysis, which allows for a more robust identification of the spectral slope and spectral regime transitions. Our results show a range of spectral slopes from -1.9 to -2.1 for the gravel bed and -2.3 to -3 for the sand bed experiments.

[60] The spectra characterize only second-order statistics of bed elevations. A higher-order statistical moments analysis of bed elevation increments (elevation differences between adjacent values) demonstrates the presence of multifractal scaling parameterized here with two parameters: the roughness and the intermittency parameter. The

roughness parameter is larger for the sand bed case, indicating a long-range dependence dominated by the presence of bed forms. The intermittency parameter is larger for the gravel bed case, suggesting a more inhomogeneous arrangement of bed elevation fluctuations, which may arise from sorting and clustering microforms intermediate in size between the grain and bed form scales. We also present evidence that the pdf's of bed elevation increments are asymmetric and have positive tails heavier than a Gaussian distribution. As the scale increases, the pdf's approach Gaussian in analogy with the pdf's of turbulent velocity fluctuations stretched at the Kolmogorov scale and approaching Gaussian at the integral scale.

[61] We use a wavelet-based scale-dependent correlation analysis to estimate the average velocity (celerity) of bed forms of various sizes and demonstrate that smaller bed forms move faster relatively to the larger bed forms. This leads to bed form superposition and coalescence and produces the multiscale structure of the bed elevation series. We are able to clearly demonstrate this in the gravel case. In the sand experiments, the elevation probes were located too far apart (order 2–3 bed forms wavelengths) to accurately estimate the scale-dependent celerity in the sand bed forms.

[62] The complex evolution of bed forms is clearly a nonlinear process and linear stability analysis has limitations in assessing the complexity and inherent lack of predictability in these series. We use a nonlinear dynamical approach (finite size Lyapunov exponent) to depict the rate of growth of finite size perturbations and estimate the predictability horizon given a specified tolerance level of uncertainty. The results demonstrate that gravel bed forms are more predictable than sand bed forms and that the predictability decreases as the rate of discharge increases.

[63] **Acknowledgments.** This research was supported by the National Center for Earth-surface Dynamics (NCED), a Science and Technology Center funded by NSF under agreement EAR-0120914, NSF grants EAR-08224084 and EAR-0835789, and a doctoral dissertation fellowship to the first author by the graduate school of the University of Minnesota. The experiments (also known as StreamLab06 and StreamLab08) were conducted at the St. Anthony Falls Laboratory as a part of an NCED program to examine physical-biological aspects of sediment transport (http://www.nced.umn.edu). The authors are thankful to Jeff Marr, Craig Hill, and Sara Johnson for providing data and information about the details of the experiments. The authors are also thankful to Christophe Ancey and two anonymous reviewers, as well as the Associate Editor, whose suggestions and constructive comments substantially improved our presentation and refined our interpretations. Computer resources were provided by the Minnesota Supercomputing Institute, Digital Technology Center, at the University of Minnesota.

References

Aberle, J., and V. Nikora (2006), Statistical properties of armored gravel bed surfaces, *Water Resour. Res.*, *42*, W11414, doi:10.1029/2005WR004674.

Aberle, J., V. Nikora, M. Henning, B. Ettmer, and B. Hentschel (2010), Statistical characterization of bed roughness due to bed forms: A field study in the Elbe River at Aken, Germany, *Water Resour. Res.*, *46*, W03521, doi:10.1029/2008WR007406.

Addison, P. S. (2002), *The Illustrated Wavelet Transform Handbook*, 353 pp., Taylor and Francis, Philadelphia, Pa.

Allen, J. R. L. (1968), *Current Ripples: Their Relation to Patterns of Water and Sediment Motion*, 433 pp., Elsevier, New York.

ASCE Task Force (2002), Flow and transport over dunes, *J. Hydraul. Eng.*, *127*, 726–728.

Aurell, E., G. Boffetta, A. Crisanti, G. Paladin, and A. Vulpiani (1996), Predictability in systems with many characteristic times: The case of turbulence, *Phys. Rev. E.*, *53*, 2337–2349.

Aurell, E., G. Boffetta, A. Crisanti, G. Paladin, and A. Vulpiani (1997), Predictability in the large: An extension of the concept of Lyapunov exponent, *J. Phys. A*, *30*, 1–26.

Barlow, J. (1959), Autocorrelation and cross correlation analysis in electroencephalography, *IRE Trans. Med. Electron.*, *6*, 179–183.

Basu, S., E. Foufoula-Georgiou, and F. Porté-Agel (2002), Predictability of atmospheric boundary-layer flows as a function of scale, *Geophys. Res. Lett.*, *29*(21), 2038, doi:10.1029/2002GL015497.

Best, J. (2005), The fluid dynamics of river dunes: A review and some future research directions, *J. Geophys. Res.*, *110*, F04S02, doi:10.1029/2004JF000218.

Blondeaux, P., and G. Seminara (1985), A unified bar-bend theory of river meanders, *J. Fluid Mech.*, *157*, 449–470.

Boffetta, G., A. Crisanti, F. Paparella, A. Provenzale, and A. Vulpiani (1998), Slow and fast dynamics in coupled systems: A time series analysis view, *Physica D*, *116*, 301–312.

Boffetta, G., M. Cencini, M. Falconi, and A. Vulpiani (2002), Predictability: A way to characterize complexity, *Phys. Rep.*, *356*, 367–474.

Butler, J. B., S. N. Lane, and J. H. Chandler (2001), Characterization of the structure of river-bed gravels using two-dimensional fractal analysis, *Math. Geol.*, *33*(3), 301–330.

Castaing, B., Y. Gagne, and E. J. Hopfinger (1990), Velocity probability density-functions of high Reynolds-number turbulence, *Physica D*, *46*, 177–200.

Coleman, S. E., and B. W. Melville (1994), Bed-form development, *J. Hydraul. Eng.*, *120*, 544–560.

Coleman, S. E., V. I. Nikora, S. R. McLean, T. M. Clunie, T. Schlicke, and B. W. Melville (2006), Equilibrium hydrodynamics concept for developing dunes, *Phys. Fluids*, *18*, 105104, doi:10.1063/1.2358332.

Colombini, M. (2004), Revisiting the linear theory of sand dune formation, *J. Fluid Mech*, *502*, 1–16.

Colombini, M., and A. Stocchino (2008), Finite-amplitude river dunes, *J. Fluid Mech.*, *611*, 283–306, doi:10.1017/s0022112008002814.

Colombini, M., G. Seminara, and M. Tubino (1987), Finite-amplitude alternate bars, *J. Fluid Mech.*, *181*, 213–232.

Crickmore, M. (1970), Effect of flume width on bed-form characteristics, *J. Hydraul. Div. Am. Soc. Civ. Eng.*, *96*, 473–496.

Defina, A. (2003), Numerical experiments on bar growth, *Water Resour. Res.*, *39*(4), 1092, doi:10.1029/2002WR001455.

Dinehart, R. L. (1992), Gravel-bed deposition and erosion by bedform migration observed ultrasonically during storm flow, North Fork Toutle River, Washington, *J. Hydrol.*, *136*, 51–71.

Dinehart, R. L. (2002), Bedform movement recorded by sequential single-beam surveys in tidal rivers, *J. Hydrol.*, *258*, 25–39.

Engelund, F., and J. Fredsøe (1982), Transition from dunes to plane bed in alluvial channels, *Ser. Pap. 4*, 56 pp., Inst. of Hydrodyn. and Hydraul. Eng., Tech. Univ. of Den., Lyngby.

Exner, F. M. (1931), Zur Dynamik der Bewegungsformen auf der Erdoberfläche, *Ergeb. Kosm. Phys.*, *1*, 373–445.

Federici, B., and G. Seminara (2003), On the convective nature of bar instability, *J. Fluid Mech.*, *487*, 125–145.

Federici, B., and G. Seminara (2006), Effect of suspended load on sandbar instability, *Water Resour. Res.*, *42*, W07407, doi:10.1029/2005WR004399.

Fernandez, F., J. Best, and F. Lopez (2006), Mean flow, turbulence structure, and bed form superimposition across ripple-dune transition, *Water Resour. Res.*, *42*, W05406, doi:10.1029/2005WR004330.

Fredsøe, J. (1974), On the development of dunes in erodible channels, *J. Fluid Mech.*, *64*, 1–16.

Frisch, U. (1995), *Turbulence: The Legacy of A. N. Kolmogorov*, Cambridge Univ. Press, New York.

Gamage, N. K. K., and W. Blumen (1993), Comparative analysis of low level cold fronts: Wavelet, Fourier, and empirical orthogonal function decompositions, *Mon. Weather Rev.*, *121*, 2867–2878.

Giri, S., and Y. Shimizu (2006), Numerical computation of sand dune migration with free surface flow, *Water Resour. Res.*, *42*, W10422, doi:10.1029/2005WR004588.

Hegger, R., H. Kantz, and T. Schreiber (1999), Practical implementation of nonlinear time series methods: The Tisean Package, *Chaos*, *9*, 413–435.

Hino, M. (1968), Equilibrium-range spectra of sand waves formed by flowing water, *J. Fluid Mech.*, *34*, 565–573.

Hudgins, L. H., C. A. Friehe, and M. E. Mayer (1993), Fourier and wavelet analysis of atmospheric turbulence, in *Progress in Wavelet Analysis and*

Applications, edited by Y. Meyer and S. Roques, pp. 491–498, Frontiers, Gif-sur-Yvette, France.

Jain, S. C., and J. F. Kennedy (1974), The spectral evolution of sedimentary bedforms, *J. Fluid Mech.*, *63*, 301–314.

Jerolmack, D. J., and D. Mohrig (2005), A unified model for subaqueous bed form dynamics, *Water Resour. Res.*, *41*, W12421, doi:10.1029/2005WR004329.

Ji, Z. G., and C. Mendoza (1997), Weakly nonlinear stability analysis for dune formation, *J. Hydraul. Eng.*, *123*, 979–985.

Julien, P., and G. Klassen (1995), Sand-dune geometry of large rivers during floods, *J. Hydraul. Eng.*, *121*, 657–663.

Kantz, H., and T. Schreiber (1997), *Nonlinear Time Series Analysis*, Cambridge Univ. Press, Cambridge, U. K.

Kennedy, J. F. (1963), The mechanism of dunes and antidunes in erodible-bed channels, *J. Fluid Mech.*, *16*, 521–544.

Klaassen, G. J. (1990), Experiments with graded sediments in a straight flume, Vol. A (Text) and Vol. B Tables and Figures, *Tech. Rep. Q788*, WL|Delft Hydraul., Delft, Netherlands.

Kumar, P., and E. Foufoula-Georgiou (1997), Wavelet analysis for geophysical applications, *Rev. Geophys.*, *35*(4), 385–412, doi:10.1029/97RG00427.

Lanzoni, S. (2000a), Experiments on bar formation in a straight flume: 1. Uniform sediment, *Water Resour. Res.*, *36*(11), 3337–3349, doi:10.1029/2000WR900160.

Lanzoni, S. (2000b), Experiments on bar formation in a straight flume: 2. Graded sediment, *Water Resour. Res.*, *36*(11), 3351–3363, doi:10.1029/2000WR900161.

Leclair, S. F. (2002), Preservation of cross-strata due to migration of subaqueous dunes: An experimental investigation, *Sedimentology*, *49*, 1157–1180.

Lorenz, E. N. (1969), The predictability of a flow which possesses many scales of motion, *Tellus*, *21*, 289–307.

Maddux, T. B., J. M. Nelson, and S. R. McLean (2003), Turbulent flow over three-dimensional dunes: 1. Free surface and flow response, *J. Geophys. Res.*, *108*(F1), 6009, doi:10.1029/2003JF000017.

Malecot, Y., C. Auriault, H. Kahalerras, Y. Gagne, O. Chanal, B. Chabaud, and B. Castaing (2000), A statistical estimator of turbulence intermittency in physical and numerical experiments, *Eur. Phys. J. B*, *16*, 549–561.

Mallat, S. (1998), *A Wavelet Tour in Signal Processing*, Academic, San Diego, Calif.

Marion, A., S. J. Tait, and I. K. McEwan (2003), Analysis of small-scale gravel bed topography during armoring, *Water Resour. Res.*, *39*(12), 1334, doi:10.1029/2003WR002367.

McElroy, B., and D. Mohrig (2009), Nature of deformation of sandy bed forms, *J. Geophys. Res.*, *114*, F00A04, doi:10.1029/2008JF001220.

Nakagawa, H., and T. Tsujimoto (1984), Spectral analysis of sand bed instability, *J. Hydraul. Eng.*, *110*(HY4), 467–483.

Nelson, J., A. R. Burman, Y. Shimizu, S. R. McLean, R. L. Shreve, and M. W. Schmeeckle (2005), Computing flow and sediment transport over bedforms, in *River, Coastal and Estuarine Morphodynamics: RCEM 2005*, edited by G. Parker and M. H. García, pp. 861–868, Taylor and Francis, Philadelphia, Pa.

Nikora, V. I., and D. G. Goring (2001), Extended self-similarity in geophysical and geological applications, *Math. Geol.*, *33*(3), 251–271, doi:10.1023/A:1007630021716.

Nikora, V., and J. Walsh (2004), Water-worked gravel surfaces: High-order structure functions at the particle scale, *Water Resour. Res.*, *40*, W12601, doi:10.1029/2004WR003346.

Nikora, V. I., A. N. Sukhodolov, and P. M. Rowinski (1997), Statistical sand wave dynamics in one-directional water flows, *J. Fluid Mech.*, *351*, 17–39.

Nikora, V. I., D. G. Goring, and B. J. F. Biggs (1998), On gravel-bed roughness characterization, *Water Resour. Res.*, *34*(3), 517–527.

Nordin, C. F., and J. H. Algert (1966), Spectral analysis of sand waves, *J. Hydraul. Div. Am. Soc. Civ. Eng.*, *92*(HY5), 95–114.

Onda, S., and T. Hosoda (2004), Numerical simulation on development process of dunes and flow resistance, in *Proceedings of Second International Conference on Fluvial Hydraulics, 23–25 June 2004, Napoli, Italy*, vol. *1*, edited by M. Greco, A. Carravetta, and R. Della Morte, pp. 245–252, Balkema, Leiden, Netherlands.

Parsons, D. R., J. L. Best, O. Orfeo, R. J. Hardy, R. Kostaschuk, and S. N. Lane (2005), Morphology and flow fields of three-dimensional dunes, Rio Parana, Argentina: Results from simultaneous multibeam echo sounding and acoustic Doppler current profiling, *J. Geophys. Res.*, *110*, F04S03, doi:10.1029/2004JF000231.

Raudkivi, A. J., and H.-H. Witte (1990), Development of bed features, *J. Hydraul. Eng.*, *116*, 1063–1079.

Schindler, R. J., and A. Robert (2004), Suspended sediment concentration and the ripple-dune transition, *Hydrol. Processes*, *18*, 3215–3227.

Schwämmle, V., and H. J. Herrmann (2004), Modelling transverse dunes, *Earth Surf. Processes Landforms*, *29*(6), 769–784.

Simons, D. B., E. V. Richardson, and C. F. Nordin Jr. (1965), Bedload equation for ripples and dunes, *U.S. Geol. Surv. Prof. Pap.*, *462-H*, 1–9.

Singh, A., K. Fienberg, D. J. Jerolmack, J. Marr, and E. Foufoula-Georgiou (2009a), Experimental evidence for statistical scaling and intermittency in sediment transport rates, *J. Geophys. Res.*, *114*, F01025, doi:10.1029/2007JF000963.

Singh, A., S. Lanzoni, and E. Foufoula-Georgiou (2009b), Nonlinearity and complexity in gravel-bed dynamics, *Stochastic Environ. Res. Risk Assess.*, *23*, 967–975, doi:10.1007/S00477-008-0269-8.

Singh, A., F. Porté-Agel, and E. Foufoula-Georgiou (2010), On the influence of gravel bed dynamics on velocity power spectra, *Water Resour. Res.*, *46*, W04509, doi:10.1029/2009WR008190.

Tjerry, S., and J. Fredsøe (2005), Calculation of dune morphology, *J. Geophys. Res.*, *110*, F04013, doi:10.1029/2004JF000171.

van der Mark, C. F., A. Blom, and S. J. M. H. Hulscher (2008), Quantification of variability in bedform geometry, *J. Geophys. Res.*, *113*, F03020, doi:10.1029/2007JF000940.

Van Rijn, L. C. (1984), Sediment transport, part III: Bed forms and alluvial roughness, *J. Hydraul. Eng.*, *110*, 1733–1754.

Venditti, J. G. (2007), Turbulent flow and drag over fixed two- and three-dimensional dunes, *J. Geophys. Res.*, *112*, F04008, doi:10.1029/2006JF000650.

Venditti, J. G., M. Church, and S. J. Bennett (2005), Morphodynamics of small-scale superimposed sand waves over migrating dune bed forms, *Water Resour. Res.*, *41*, W10423, doi:10.1029/2004WR003461.

Venugopal, V., S. G. Roux, E. Foufoula-Georgiou, and A. Arneodo (2006), Revisiting multifractality of high-resolution temporal rainfall using a wavelet-based formalism, *Water Resour. Res.*, *42*, W06D14, doi:10.1029/2005WR004489.

Wilbers, A. W. E. (2004), *The Development and Hydraulic Roughness of Subaqueous Dunes*, Ph.D. thesis, 224 pp., Fac. of Geosci., Utrecht Univ., Utrecht, Netherlands.

Wilbers, A. W. E., and W. B. M. ten Brinke (2003), The response of subaqueous dunes to floods in sand and gravel bed reaches of the Dutch Rhine, *Sedimentology*, *50*, 1013–1034, doi:10.1046/j.1365-3091.2003.000585.x.

Wong, M., G. Parker, P. DeVries, T. M. Brown, and S. J. Burges (2007), Experiments on dispersion of tracer stones under lower-regime plane-bed equilibrium bed load transport, *Water Resour. Res.*, *43*, W03440, doi:10.1029/2006WR005172.

Yarnell, S. M., J. F. Mount, and E. W. Larsen (2006), The influence of relative sediment supply on riverine habitat heterogeneity, *Geomorphology*, *80*, 310–324.

E. Foufoula-Georgiou and A. Singh, St. Anthony Falls Laboratory, Department of Civil Engineering, University of Minnesota, Twin Cities, Minneapolis, MN 55414, USA. (efi@umn.edu)

S. Lanzoni, Department IMAGE, University of Padova, via Loredan 20, I-35131 Padova, Italy.

P. R. Wilcock, Department of Geography and Environmental Engineering, Johns Hopkins University, Baltimore, MD 21218, USA.